POLITECNICO
MILANO 1863

SCUOLA DI INGEGNERIA INDUSTRIALE
E DELL'INFORMAZIONE

Aeroacoustic characterization of a 3D organ pipe

Tesi di Laurea Magistrale in
Aeronautical Engineering - Ingegneria Aeronautica

Óscar Martínez Díaz, 958843

Advisor:
Prof. Paolo Schito

Co-advisor:
Alberto Artoni

Academic year:
2021-2022

Abstract: The aeroacustic field of an organ pipe is investigated numerically. The compressible Navier-Stokes equations are solved by employing a Large Eddy Simulation turbulence model implemented in the open source library OpenFOAM. Then to compute the far field noise we make use of the Ffowcs Williams and Hawkings acoustic analogy. The objective of the thesis is to perform a computational simulation of a three-dimensional organ pipe. First, the computational methodology is validated on a two-dimensional test case, namely the noise induced by a laminar flow over a square cylinder. Then a 2D organ pipe model is considered where the numerical setup is tested following Fischer *et al.* The two-dimensional case is also used to study the fluid mechanisms that generate the sound, focusing on the coupling mechanism and behavioural changes due to modifications of the geometry. The results obtained from the three-dimensional model are compared with the two-dimensional case. The SPL-spectra of the acoustic far field are obtained using an acoustic analogy and compared between the cases and with the measurements on real organ pipes.

Key-words: Aeroacoustics, OpenFOAM, organ pipe, Ffowcs Williams and Hawkings, FWH, 3D, CFD, Large eddy simulation, LES, libAcoustics

Contents

1. Introduction

Aeroacoustics is the field of acoustics that studies the noise induced by fluid flows. It was first studied by Lighthill [1, 2] in the mid-twentieth century, originally to address the noise generated by jet engines. First, Lighthill derived an exact acoustic inhomogeneous equation from the mass and momentum compressible Navier-Stokes equations that contained the noise generated by the flow. Then, the inhomogeneus wave equation was solved by employing the Green function theory. Curle [3] considered the same wave equation but he employed a generalised Kirchoff integral to obtain the solution. In this way only the noise generated by the aerodynamic forces is considered. Later, Ffowcs Williams and Hawking [4] extended the Curle strategy in order to consider moving surfaces.

A fascinating field in which aeroacoustic can provide more insight on the physical mechanism of sound generation and propagation is musical acoustics. The air flow in musical instruments is a long standing problem in the field of musical acoustics due to the highly complex underlying physics that often involves multi-physics problems [5].

Musical instruments are usually classified by the way sound is produced: string, wind, percussion, and electronic instruments. Wind instruments are typically grouped into two families: brass and woodwind. Nevertheless, from a fluid dynamic point of view they are better classified as reed instruments and flue instruments. A reed is a flexible element that oscillates due to a flow-induced vibration (flutter). Flue instruments are wind instruments in which sound is produced by flow instability without significant wall vibration, and hence the wall can be considered rigid [6]. In organ pipes the flow instability comes from an air jet impinging a sharp edge. This creates an acoustical excitation that then propagates inside the organ pipe, which acts as an acoustic resonator [7].

Since the 1960s [8–10], a phenomenological theory that characterises the behaviour of flue instruments has been established in the field of musical acoustics. However, the theory created in the area of musical acoustics is far from rigorous and contains numerous conceptual approximations, using semiempirical lumped models and assuming an incompressible frictionless flow with singular vortical structures, such as vortex sheets or point vortices [6]. Although such lumped models can be used to create virtual instruments, they cannot explain the importance of the geometric details of the mouth for the playability and sound quality of musical instruments. For flue instruments, a rigorous theory must be based on the Navier-Stokes equations of fluid dynamics and it should take into account the function the flow field as a sound source in the intricate instrument architecture. To best understand the sound generation and propagation mechanism, it was decided to study the process through its fluid dynamics, using the traditional tools this field provides together with more ad hoc aeracoustics numerical tools.

The final goal of this work is to study and validate the methodology to correctly perform a three-dimensional computational experiment of the turbulent fluid flow and the coupled acoustic field created by a flue pipe musical instrument, particularly an organ pipe. The main reference for this work are those developed by Fischer *et al.* [11–13], in which a two-dimensional computational simulation of the fluid flow around a organ pipe was compared with experimental results, analysing also the effect of the sound reflections due to changes on the room geometry. A similar experiment was performed by Miyamoto *et al.* [14], studying the effects of jet changes on the frequency of the sound on both two-dimensional and quasi-two-dimensional simulations. A more complex simulation was done by Kobayashi *et al.* [15]: a three-dimensional case calculation of the compressible turbulent flow around a flue-like instrument, in this case an ocarina.

The thesis is organised as follows. In Section 2, the methodology used is reviewed. First, the Navier-Stokes equations are introduced, followed by a brief review of Large Eddy Simulation modelling and finishing with an introduction to the aeroacoustic analogies. Section 3.2 consists of all the numerical results obtained, starting with the validation of the methodology through a simple aeroacoustic case, namely the laminar flow around a

squared cylinder. Next, we simulate the flow of a two-dimensional organ pipe, with comparison to the results obtained by Fischer *et al.* [13]. We then consider the final three-dimensional organ pipe, where we employ the same modelling and numerical strategy of the two-dimensional case. Comparisons between the cases and the experiments are made to extract some validation and differences between the cases. Finally, Section 4 concludes the thesis with a summary and the conclusions obtained from the obtained results.

2. Methodology

In this section, the theory and the methodology used in this work are reviewed. First, a recall of the basic equations of fluid dynamics, followed by some basic LES turbulence modelling and finally introducing the main aeroacoustic models and computational strategies.

2.1. Fluid dynamics

The flow in an organ pipe and its acoustic field are described by the general laws of motion of fluids, which obey the fundamental laws of conservation, also known as the Navier-Stokes equations:

$$\begin{aligned} \frac{\partial \rho}{\partial t} + \nabla \cdot (\rho \mathbf{u}) &= 0\,, && \text{(continuity)} \\ \frac{\partial \rho \mathbf{u}}{\partial t} + \nabla \cdot (\rho \mathbf{u} \otimes \mathbf{u}) &= -\nabla \mathcal{P}\,, && \text{(momentum balance)} \\ \frac{\partial}{\partial t}\Big[\rho\Big(e + \frac{u^2}{2}\Big)\Big] + \nabla \cdot \Big[\rho \mathbf{u}\Big(e + \frac{u^2}{2}\Big)\Big] &= -\nabla \cdot \Big[\mathcal{P} \cdot \mathbf{u} + \mathbf{q}\Big]\,, && \text{(energy balance)} \end{aligned} \tag{1}$$

where ρ is the fluid density, $\mathbf{u}$ is the flow velocity, e is the internal energy per unit mass, u is the speed, namely $u = |\mathbf{u}|$; $\mathbf{q} = -\kappa \nabla T$ is the heat flux, κ is the thermal conductivity and T the temperature, [16]. Finally, $\mathcal{P} = p\mathcal{I} - \sigma$ is the stress tensor, whose isotropic part $p\mathcal{I}$ corresponds to the effect of the hydrodynamic pressure $p = \mathcal{P}_{ii}/3$, and its deviation from the hydrostatic behaviour $\sigma_{\mathbf{ij}} = \mu[\frac{\partial u_i}{\partial x_j} + \frac{\partial u_j}{\partial x_i} - \frac{2}{3}(\nabla \cdot \mathbf{u})\delta_{ij}] + \mu_v(\nabla \cdot \mathbf{u})\delta_{ij}$ corresponds in a simple fluid to the effect of viscosity. We define a simple fluid as a fluid for which σ is symmetrical. μ is the dynamic viscosity, μ_v is the bulk viscosity and δ is the Dirac delta.
The flow is identified by employing non-dimensional numbers, such as the Reynolds number, defined as the dimensionless ratio of inertial forces to viscous forces $Re = \frac{\rho U L}{\mu} = \frac{UL}{\nu}$, the Prandtl number, defined as the ratio of momentum diffusivity to thermal diffusivity $Pr = \frac{\nu}{\alpha} = \frac{c_p \mu}{\kappa}$, and the Mach number, which is defined as the ratio between the flow velocity and the speed of sound: $Ma = \frac{U}{c}$.
In this equations U is a fluid flow characteristic velocity, L is a geometrical characteristic length, $\nu = \mu/\rho$ is the kinematic viscosity, α is the thermal diffusivity, c_p is the specific heat, and c is the speed of sound. At low Reynolds numbers, the flow is said to be laminar. This behaviour is ordered, the flow structures are big and periodic. Increasing the Reynolds number, the behaviour of the flow tends to be more chaotic and disordered. Structures are smaller at larger Reynolds number. Here the flow is said to be turbulent. A main feature of turbulence is, in comparison against laminar flow, its ability to transport and mix fluid much more effectively. Although turbulent flows are very complex, they dominate most of the natural phenomena such as transport and mixing of matter, momentum, and heat in flows; which is of great practical importance [17].

2.2. Turbulence modelling: Large Eddy Simulation

Doing a Direct Numerical Simulation or DNS of the Navier-Stokes equations, where all the length scales of the fluid are solved, is too computationally expensive. The minimum grid space required to solve all the turbulent length scales in a flow field scales as $Re^{-9/4}$, and for high Reynolds number may be too small, creating a computational grid with too many elements, and consequently computational expensive, for moderate Reynolds numbers. The main objective of turbulent models is to reduce the scales that have to be explicitly resolved, and model the smaller scales.
In Large Eddy Simulation (LES), smaller-scale motions are modelled, whereas the larger unsteady turbulent motions are represented exactly. Since larger scales have to be resolved, while the smaller are modelled, the grid employed in LES computation is coarser than the one required by a DNS, reducing the overall computational cost. To achieve this, in LES a low-pass filtering operation is performed. The filtering is performed as follows:

$$\begin{cases} \phi = \overline{\phi} - \phi' \\ \overline{\phi}(\mathbf{x}, t) = \displaystyle\int_{-\infty}^{+\infty} \int_{-\infty}^{+\infty} \phi(\mathbf{r}, \tau) G(\mathbf{x} - \mathbf{r}, t - \tau) d\mathbf{r} d\tau \end{cases}$$

where ϕ is the flow field being filtered with its spatial $\mathbf{x}$ and temporal t dependence, $\overline{\phi}$ is the filtered field, G is the specified filtering function, and ϕ' is the residual field. LES avoids the need to rely on a closure scheme to parameterise the large eddies, while simultaneously circumventing the restrictions imposed by the high computational cost of the smaller ones.
Filtering the Navier-Stokes equations, one obtains:

$$\frac{\partial \rho}{\partial t} + \nabla \cdot (\rho \overline{\mathbf{u}}) = 0 \,, \qquad \text{(continuity)}$$

$$\frac{\partial \rho \overline{\mathbf{u}}}{\partial t} + \nabla \cdot (\rho \overline{\mathbf{u}} \otimes \overline{\mathbf{u}}) = -\nabla \overline{\mathcal{P}} - \nabla \tau \,, \qquad \text{(momentum balance)}$$

$$\frac{\partial}{\partial t}\Big[\rho\Big(e + \frac{\overline{u}^2}{2}\Big)\Big] + \nabla \cdot \Big[\rho \overline{\mathbf{u}}\Big(e + \frac{\overline{u}^2}{2}\Big)\Big] = -\nabla \cdot \Big[\overline{\mathcal{P}} \cdot \overline{\mathbf{u}} + \tau \cdot \overline{\mathbf{u}} + \mathbf{q}\Big] \,, \qquad \text{(energy balance)}$$

$$\tau = \rho \overline{\mathbf{u} \otimes \mathbf{u}} - \rho \overline{\mathbf{u}} \otimes \overline{\mathbf{u}} \,. \qquad \text{(subgrid-scale stress)}$$

In order to close the equations for the filtered velocity, a model for τ is needed. Currently, the most popular subgrid-scale model is the algebraic eddy viscosity model originally proposed by Smagorinsky [18]:

$$\tau_{ij} = -2\nu_{SGS}\overline{D}_{ij} + \frac{1}{3}\delta_{ij}\tau_{kk} \,,$$

where ν_{SGS} is the subgrid-scale eddy viscosity, and

$$\overline{D}_{ij} = \frac{1}{2}\Big(\frac{\partial \overline{u}_i}{\partial x_j} + \frac{\partial \overline{u}_j}{\partial x_i}\Big) \,,$$

is the resolved scale strain rate tensor. For the modelling of τ in this work, the attention is focused on the one-equation model of the transport of turbulent kinetic energy k developed from the work of Yoshizawa [19]. The turbulent kinetic energy is split up into a grid-scale term k_{GS}, that is solved, and a subgrid-scale term k_{SGS}, objective of the turbulence model. The model equation for the subgrid-scale turbulent kinetic energy is:

$$\tau_{ij} = -2\nu_{SGS}\overline{S}_{ij} + \frac{2}{3}\delta_{ij}k_{SGS} \,,$$

$$\nu_{SGS} = C_k k_{SGS}^{1/2}\Delta$$

$$-\rho\tau_{ij} : \overline{D}_{ij} - C_\epsilon \frac{\rho k_{SGS}^{3/2}}{\Delta} = \frac{\partial(\rho k_{SGS})}{\partial t} + \frac{\partial(\rho \overline{u}_j k_{SGS})}{\partial x_j} - \frac{\partial}{\partial x_j}\Big[\rho(\nu + \nu_{SGS})\frac{\partial k_{SGS}}{\partial x_j}\Big] \,,$$

$$-\tau_{ij} : \overline{D}_{ij} = -\frac{2}{3}k_{SGS}\frac{\partial \overline{v}_k}{\partial x_k} + \nu_{SGS}\frac{\partial \overline{u}_i}{\partial x_j}\Big(2\overline{D}_{ij} - \frac{1}{3}tr(2\overline{D})\delta_{ij}\Big) \,, \qquad \text{(production term)}$$

where $C_\epsilon = 1.048$ and $C_k = 0.094$ are model constants, and Δ is the grid resolution.

2.3. Computational fluid dynamics

Computational fluid dynamics or CFD is the analysis of systems involving fluid flow, heat transfer and associated phenomena such as chemical reactions by means of computer-based simulation [20].
To deal with the CFD experiments of this thesis, the software OpenFOAM [21] was used, a C++ toolbox for the development of customised numerical solvers. The finite volume method [22] is used for the discretisation. The numerical solvers used in this thesis are:

- `rhoCentralFoam`: based on the central-upwind schemes of Kurganov and Tadmor, this solver is compressible, transient, density based, and shock capturing [23].
- `rhoPimpleFoam`: Compressible, transient solver based on the PIMPLE algorithm, a combination of the PISO (Pressure Implicit with Splitting of Operators) and SIMPLE (Semi-Implicit Method for Pressure Linked Equations) algorithms [24].

The Dirichlet boundary conditions will be indicated as `fixedValue`, namely a value will be enforced on the boundary. `zeroGradient` will denote a boundary condition that enforces a Neumann-like boundary condition. The `inletOutlet` boundary conditions sets the value to the a specified fixed value for reverse flow and the outflow is treated using a `zeroGradient` condition.
Acoustic (and also compressible) external problems require also particular non-reflecting boundary conditions, in order to avoid spurious reflection that the boundary might induce. The `waveTransmissive` boundary conditions impose a Poinsot-Lele-like [25] allows to properly transmit the outgoing wave. This boundary condition determines the boundary value by solving the material derivative equation

$$\frac{D\phi}{Dt} = \frac{\partial \phi}{\partial t} + \mathbf{U} \cdot \nabla \phi = \frac{\partial \phi}{\partial t} + U_n \cdot \frac{\partial \phi}{\partial \mathbf{n}} = 0 \,,$$

where ϕ is a flow field variable, $\mathbf{n}$ is the vector normal to the surface, and $\mathbf{U}$ is the advection velocity that can be assumed to be normal to the surface as U_n. This normal advection velocity is calculated as

$$U_n = \frac{\phi_p}{|\mathbf{Sf}|} + \sqrt{\frac{\gamma}{\psi_p}}\,.$$

where ϕ_p is face flux, $\psi_p = \rho/p$ is the local compressibility, $\mathbf{Sf}$ is the face area vector, and γ is ratio of specific heats.

2.4. Computational aeroacoustics

Computational aeroacoustics (CAA) aims to solve the aeroacoustic problems by employing numerical methods. The compressible Navier-Stokes equations describe the fluid flow, and therefore the generated aeroacoustical field, but when simulating turbulent flows the cost of the simulation is too much demanding. Hybrid methods exist as a more affordable way to compute the acoustic far field. This methods first solve the flow field using a standard CFD solver and they solve the acoustic problem through other methods most suitable and more affordable computationally. Usually the acoustic solvers are based on integral methods, typically based on the acoustic analogy.

2.4.1 Lighthill

The key idea of Lighthill [1, 2] is to manipulate the Navier-Stokes equations (1). By taking the time derivative of the continuity, subtracting the divergence of the momentum balance equation, and subtracting the term $c_0^2\Delta p'$, the equations turn into an inhomogeneous wave equation whose inhomogeneous term plays the role of the source.

$$\frac{\partial^2 \rho'}{\partial t^2} - c_0^2 \frac{\partial^2 \rho'}{\partial x_i^2} = \frac{\partial^2 T_{ij}}{\partial x_i \partial x_j} \tag{2}$$

in which the subscript $\cdot_0$ indicates the undisturbed flow, $\rho' = \rho - \rho_0$ is the density acoustic perturbation, defined as the difference between the density and the reference density of the undisturbed medium; $T_{ij} = \rho u_i u_j - \sigma_{ij} + (p' - c_0^2\rho')\delta_{ij}$ is the Lighthill's stress tensor; and $\sigma_{ij} = p\delta_{ij} - \mathcal{P}_{ij}$ is the deviation from the hydrostatic behaviour, which corresponds in a simple fluid to the effect of viscosity.
Equation (2) can be solved analytically by employing a convolution between the source and a suitable Green function. The Green's function of the free field radiation reads:

$$G(\mathbf{x}, t) = \frac{\delta(t - \tau - r/c_0)}{4\pi r}\,, \tag{3}$$

where τ is the retarded time and r is the distance between the observer and the source. By using the Green function in Equation (3), it is possible to solve Equation (2) obtaining the following integral form:

$$\rho' = \frac{1}{4\pi c_0^2} \frac{\partial^2}{\partial x_i \partial x_j} \int_\Omega \frac{T_{ij}(\mathbf{y}, \tau)}{|\mathbf{x} - \mathbf{y}|} d\Omega(\mathbf{y})$$

where Ω is the control volume as the instant in which the acoustic radiation is emitted from the position $\mathbf{y}$ that is where the sound source is placed.

2.4.2 Curle

Lighthill's analogy can be generalised for flows in the presence of walls. Curle [3] modified Lighthill assumption considering the presence of a solid boundary. A fixed surface Σ is considered with outer normal $\mathbf{n}$ and Green's theorem is applied to the volume Ω outside of Σ. By means of partial integration and utilising the symmetry properties of the Green's function:

$$p' = \frac{\partial^2}{\partial x_i \partial x_j} \int_\Omega \Big[\frac{T_{ij}}{4\pi r}\Big] d\Omega + \int_\Sigma \Big[\frac{\partial}{\partial t}\Big(\frac{\rho u_i}{4\pi r}\Big) - \frac{\partial}{\partial x_j}\Big(\frac{\mathcal{P}_{ij} + \rho u_i u_j}{4\pi r}\Big)\Big] n_i d\Sigma$$

2.4.3 Ffowcs Williams and Hawkings

Ffowcs Williams and Hawkings (FWH) introduced [4] some variations into Lighthill analogy, considering also the presence of solid boundaries and the motion of a body. While Curle's formulation discussed in the previous

section assumes a fixed control surface Σ, the FWH allows the use of a moving control surface $\Sigma(t)$. This is achieved defining a volume $\Omega(t)$ enclosed by $\Sigma(t)$ and a smooth function $f(\mathbf{x}, t) = 0$ such that

$$\left.\begin{aligned} f(\mathbf{x},t) < 0 \text{ if } \mathbf{x} \in \Omega(t) \\ f(\mathbf{x},t) = 0 \text{ if } \mathbf{x} \in \Sigma(t) \\ f(\mathbf{x},t) > 0 \text{ if } \mathbf{x} \notin \Sigma(t) \wedge \mathbf{x} \notin \Omega(t)\ . \end{aligned}\right\}$$

Now consider any physical quantity defined outside $\Omega(t)$, and extend its definition to all space by giving it a value equal to zero inside $\Omega(t)$. This can be done multiplying the variable assigned to the physical quantity by the Heaviside function $H(f)$. Introducing this into the mass and momentum equations, following Lighthill's procedure, and applying Green's theorem and using the free-space Green's function, the FWH equation, as originally proposed in [4], is:

$$\Box^2 p' = \frac{\partial}{\partial t}(\rho_0 u_n \delta(f)) - \frac{\partial}{\partial x_i}(p\, n_i \delta(f)) + \frac{\partial^2}{\partial x_i \partial x_j}(H(f) T_{ij}) \tag{4}$$

where $\Box^2$ is the D'Alambertian operator in three dimensional space, and $f(\mathbf{x}, t) = 0$ describes the moving surface. The symbol u_n denotes the local normal velocity of the surface. Finally, the Dirac and the Heavyside delta functions are denoted $\delta(f)$ and $H(f)$, respectively.

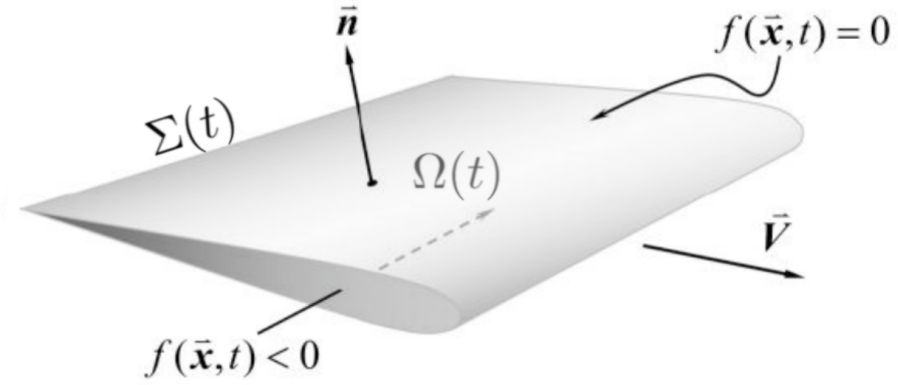

Figure 1: The definition of the moving surface implicitly as $f(\mathbf{x}, t) = 0$. Note that $\nabla f = \mathbf{n}$ where $\mathbf{n}$ is the unit outward normal to the surface [26]. $\vec{\mathbf{V}}$ is the velocity of the moving surface.

Farassat [27] and Brentner [28] developed integral representations of Equation 4 using the free-space Green's function given by Equation 3. Given geometry, motion, and surface loadings, these representation allow to solve the acoustic problem. These integral representations are valid for general motions in both subsonic and supersonic flow. Shown here is the equation for the FWH-Farrassat 1A formulation [26]:

$$\begin{aligned} 4\pi p'(\mathbf{x},t) = 4\pi(p'_T(\mathbf{x},t) + p'_L(\mathbf{x},t)) = \int_{f=0} \Big[\frac{\rho_0 \dot{u_n}}{r(1-M_r)^2} + \frac{\rho u_n \hat{r}_i \dot{M}_i}{r(1-M_r)^3}\Big]_{ret} d\Sigma + \\ \int_{f=0} \Big[\frac{\rho_0\, c\, u_n (M_r - M^2)}{r^2(1-M_r)^3}\Big]_{ret} d\Sigma + \int_{f=0} \Big[\frac{\dot{p}\cos\theta}{cr(1-M_r)^2} + \frac{\hat{r}_i \dot{M}_i p \cos\theta}{cr(1-M_r)^3}\Big]_{ret} d\Sigma + \\ \int_{f=0} \Big[\frac{p(\cos\theta - M_i n_i)}{r^2(1-M_r)^2} + \frac{(M_r - M^2) p \cos\theta}{r^2(1-M_r)^3}\Big]_{ret} d\Sigma \end{aligned}$$

where the subscript $\cdot_{ret}$ indicates evaluation at the *retarded time* (when the source sends the information the observer) respectively. r is the distance between source and observer, M_r is the Mach number in the radiation direction, θ is the local angle between the normal to the surface and the radiation direction, $\mathbf{r}$ at the emission time and c is the speed of sound. The superscripts $\hat{\cdot}$ and $\dot{\cdot}$ indicate unit vector and time derivative (with respect to observer time).
The first two integrals correspond to the thickness noise p'_T, whereas the last two integrals define the loading noise p'_L, which are monopole-like and dipole-like sources. The terms are separated into near field terms $(1/r^2)$ and far field terms $(1/r)$.
In this thesis, aeroacustics of the far field are computed using the third-party open-source library `libAcoustics` [29] of OpenFOAM [21], which using the Farassat's Formulation 1A of the FWH to compute the fluctuating pressure obtained by an observer outside the domain.

3. Numerical Results

The aim of this thesis is to provide an understanding of the computational aeroacoustics obtained using OpenFOAM in different cases of increasing complexity, studying the sound emission and propagation.

3.1. Square cylinder

The flow around a square cylinder is one of the typical problems of flow around bluff body, and a number of studies on the flow around rectangular cylinders have been done both experimentally and computationally. Inoue *et al.* [30] studied the generation mechanism of the sound in a uniform flow radiated by the flow past this geometry, performing a Direct Numerical Simulation (DNS) of the two-dimensional unsteady compressible Navier-Stokes equations. Ali *et al.* [31] performed a study on the sound generated by a square cylinder with a splitter plate at low Reynolds number, using acoustic analogies to study the aeroacoustic flow in the far field.

3.1.1 Flow specifications

A rigid square cylinder immersed in a compressible, unsteady, laminar flow at Mach number $Ma = 0.2$, with a Reynolds number of $Re = U_\infty D/\nu = 150$, a Prandtl number of $Pr = 0.75$, and a ratio of specific heats $\gamma = 1.4$ is considered. The fluid is considered a perfect gas $\rho = p/(RT)$, with R being the universal gas constant.The problem is resolved by the finite volume discretisation approach on which OpenFOAM is based.

3.1.2 Numerical setup

Different studies [30] suggest than the three-dimensional disturbances that cause the transition from a two-dimensional flow to a three-dimensional flow occur at $Re > 160$, therefore this case with $Re = 150$ can be considered two-dimensional. The stationary flow is achieved after a non-dimensional computational time of $TU_\infty/D \approx 400$, using a non-dimensional time step of $\Delta t U_\infty/D \approx 2 \times 10^{-4}$ to keep the CFL number under 1. The simulation is carried on using the solver `rhoCentralFoam` using the following numerical schemes:

- 2^{nd} order backward scheme for temporal discretization (BDF2).

$$\frac{\partial}{\partial t}\phi^n = \frac{1}{\Delta t}\left(\frac{3}{2}\phi^n - 2\phi^{n-1} + \frac{1}{2}\phi^{n-2}\right) \tag{5}$$

- For the convection term, a second-order central differences Total Variation Diminishing and Normalised Variable Diagram scheme [32]. The face flux is calculated as the average of the two adjacent nodes.
- OpenFOAM uses bases all the schemes for the viscous term on the Gauss theorem. On top of that, the chosen interpolation scheme is an unbounded, 2^{nd} order (adds an explicit non-orthogonal correction to maintain second-order accuracy), conservative linear scheme. An explicit non-orthogonal correction is made for the non-isotropic part of the mesh.

Computational domain The computational domain is generated taking as origin the centre of the square cylinder and extending in a circular shape to a radius of $150D$. By looking at Figure 2 the air flows following the direction of the positive x axis shown in Figure 2, crossing the square cylinder.

Boundary conditions To numerically solve the compressible Navier-Stokes equations used to model this problem is necessary to define the boundary conditions for the pressure, velocity and temperature. For the pressure, the inlet and the outlet are defined as non-reflective boundary conditions, and Neumann-like boundary conditions are set for the cylinder. The velocity and the temperature have Dirichlet boundary conditions for both the inlet and the cylinder, and a mix of Dirichlet-like and Neumann-like for the outlet. All the boundary conditions are listed in table 1.

	Inlet	Outlet	Cylinder
p	`waveTransmissive`	`waveTransmissive`	`zeroGradient`
U	`fixedValue`	`inletOutlet`	`fixedValue`
T	`fixedValue`	`inletOutlet`	`fixedValue`

Table 1: Boundary conditions for the laminar square cylinder.

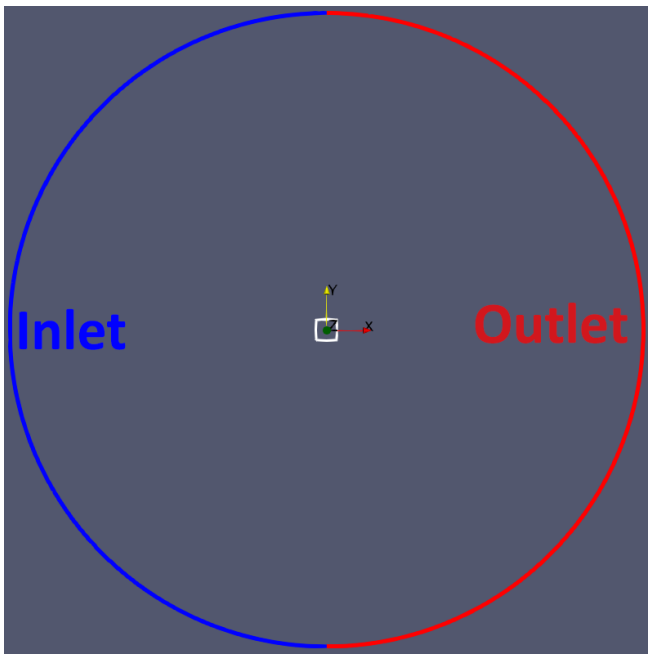

Figure 2: Flow domain for the square cylinder laminar case. The inlet is in blue. The outlet is in red. The square cylinder (white) is at the centre of the domain.

Mesh In this study, a grid with 800×675 cells is created, in the polar and radial directions respectively, generating a completely structured grid of hexahedra. The grid is divided in two areas: from the outside boundaries $r = 150D$ until $r = 25D$ the mesh is uniformly distributed in both the radial and polar coordinates; from $r = 25D$ until the square cylinder is reached, the cells get smaller the closer they are to the object, reaching a smaller cell of size $\Delta y = 3.57 \cdot 10^{-2} D$. To properly perform a DNS, the smallest cell size needed is proportional to $Re^{-3/4} D$, which for this case would be of $\Delta y = 2.33 \cdot 10^{-2} D$, approximately 0.65 of the current smallest size. It is important to have a fine mesh near the cylinder, as capturing the wake and the initial pressure waves is of utter importance to get the correct results.

3.1.3 Results of the methodology assessment

The unsteady laminar flow crossing the square cylinder is characterised by separation starting from the upper corners of the geometry. This phenomenon, at $Re = 150$, generates vortices in the wake of the cylinder, resulting in the so called Von Karman street that can be seen in Figure 3a.

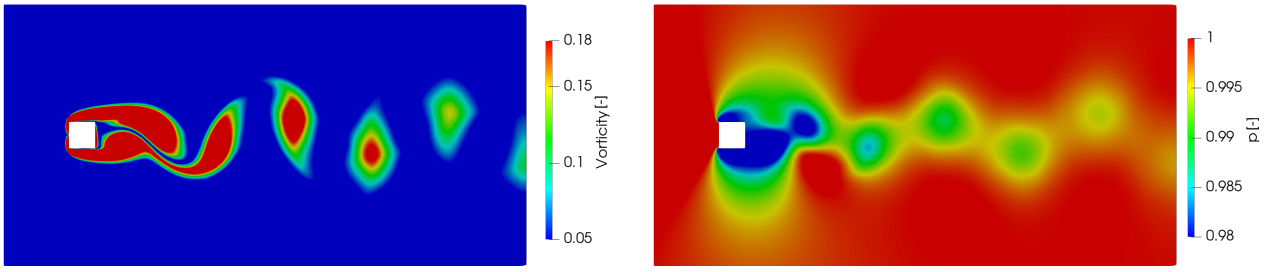

(a) (b)

Figure 3: Instantaneous non-dimensional vorticity and pressure fields around the square cylinder at $TU/D = 390$.

From Figure 4a that, during the period $TU/D \approx 389 - 393$, the lift coefficient C_l takes a negative value with its peak at $TU/D \approx 390$. The vorticity field in Figure 3a shows that a vortex is shed from the lower side of the square cylinder during this period. The amplitude of the lift coefficient is larger than that of the drag coefficient C_d (Figure 4a) and the frequency of the latter is twice as high as that of C_l (Figure 4b).

The frequency of the pressure waves is the same as that of vortex shedding as well as the fluctuation frequency of the lift force. Is it possible to define the Strouhal number as $St = fD/U_\infty$, where f is the Strouhal frequency.

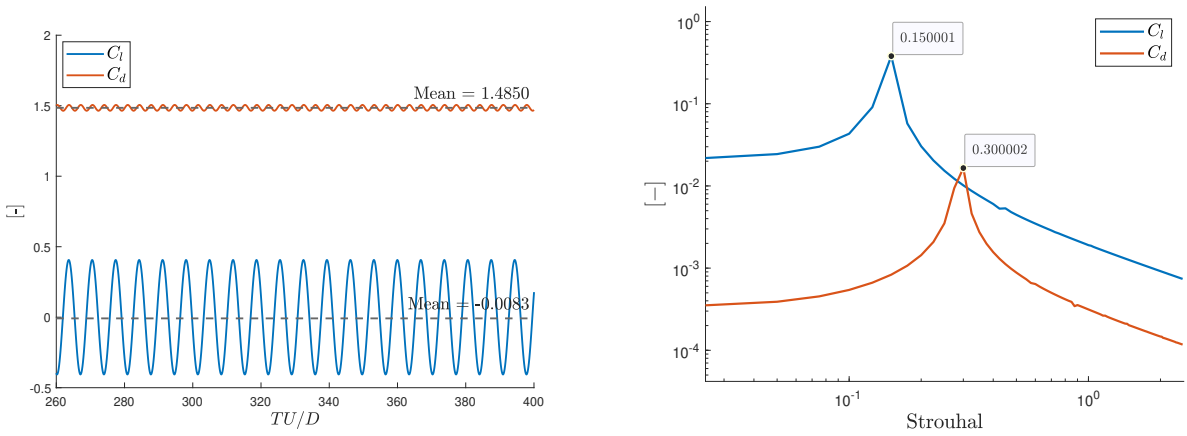

(a) (b)

Figure 4: Time histories of drag and lift coefficient and single-sided amplitude spectrum of the force coefficients.

Important obtained results of the simulation are on display on Table 2 compared with the literature. Here it can be seen how similar the fluid dynamic quantities are. The computed mean drag and lift coefficient are in agreement with the literature results. Also the peaks ΔC_l and ΔC_d match the reference. It is important to mention the slight overshoot that the results have with respect to the DNS performed by Inoue *et al.*.

	Results	**Inoue *et al.* [30]**
St	0.150	0.1512
$C_{d,mean}$	1.4850	1.414
ΔC_d	0.0207	0.0204
$C_{l,mean}$	-0.0083	0
ΔC_l	0.4063	0.3923

Table 2: Comparison of the performed case with the previous study.

On Figure 5 the dimensionless acoustic pressure $p' = \frac{p-\langle p \rangle}{\gamma U_\infty^2}$ flow field obtained can be seen, where $\langle p \rangle$ is the time averaged pressure. The generated sound has a dipolar nature; and from the results shown on Table 2 it can be seen that the lift dipole dominates the sound field.
A polar plot containing p_{rms}, the root mean square of p', namely $\sqrt{\langle p'^2 \rangle}$, is now shown to investigate the nature of the sound in the far field. Specifically, the pressure directivities are shown in Figure 6, with data collected from a total of 64 probes positioned on the flow field, equally separated on the polar coordinate at a radius of $75D$ from the centre of the square cylinder. Figure 6 show that the results of Inoue *et al.* have a directivity of 95°, where for the experimental results it is located at 99.7°. It is clear that this approach ensures a good reconstruction of the acoustic far field, with a difference in the direction of the maximum sound pressure level of less than 5°. The directivity pattern is that of a dipole, with only a slight overshoot of the sound intensity with respect to the DNS from the literature, registering a maximum in p_{rms} of 37.2 dB against the 37.0 dB of the reference, coinciding with that registered on Table 2. The small deviation in the upstream between the results from Ali *et al.* is due to the Doppler effect (taken in the moving frame), which is not taken into account in Ali *et al.*'s study [31].

3.2. Two-dimensional organ pipe

The aeroacoustic behaviour of an organ pipe is now considered. It is important to understand and visualise the fluid dynamic mechanisms by which flue instruments generate sound and the generated frequency. Fabre *et al.* establish the necessity of studying particularly this type of instruments, as reasonable analytical models are available for reeds, lips, and vocal folds, but not for flue instruments, as their complex behaviour escapes a simple universal description [6].

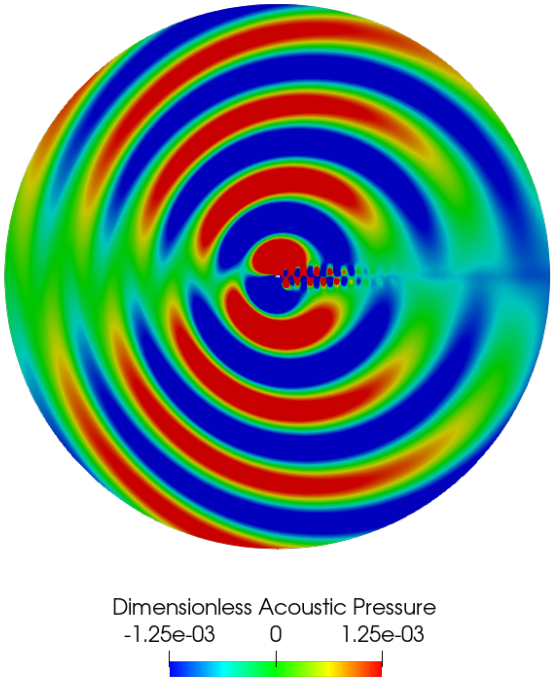

Figure 5: Dimensionless acoustic pressure at $TU/D = 400$.

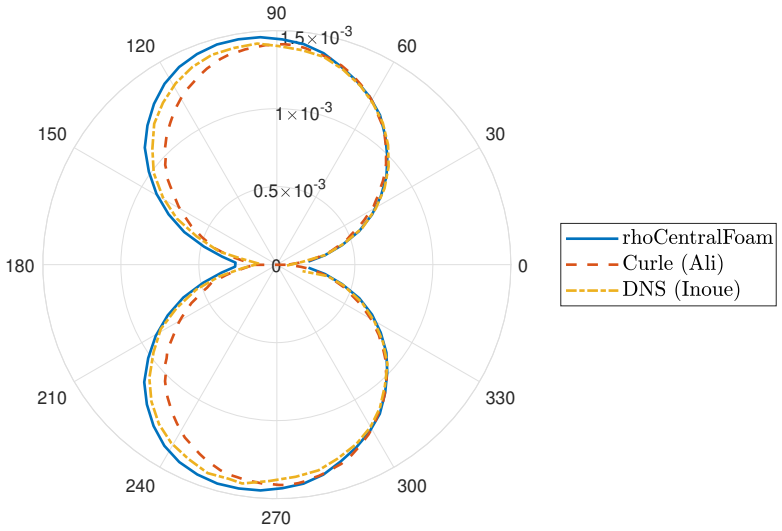

Figure 6: Directivities of the dimensionless root mean square sound pressure.

Different computational experiments have been made to study the aeroacoustics and the flow of this instruments. Those of particular interest are the two-dimensional CFD simulations performed by Fischer *et al.* [13], in which this section of the thesis is based, Miyamoto *et al.* [14], and Sorini's Master thesis [33].
The scope of this section is to create and study a two-dimensional model before moving into the more complex and difficult three-dimensional case.

3.2.1 Flow specifications

The geometry that the flow traverses is obtained from a stopped wooden organ pipe, produced by the German organ builder Alexander Schuke Orgelbau GmbH [34] and obtained from the study performed by Fischer *et al.* [13]. In particular, the two-dimensional computational grid consists of an inlet of 0.6 mm with a distance of 5.5 mm between the jet and the leading edge of the pipe's resonator. This last part has a length of 106 mm and a height of 9.5 mm. The resonator has solid walls of 6 mm of width, as seen in Figure 7. Initially, the flow is static, with an initial pressure of $p_0 = 101325$ Pa, a temperature of $T_0 = 293$ K, a kinematic viscosity

of $\nu = 1.53 \cdot 10^{-5}\ m^2/s$. From the inlet, the flow jet velocity is 18 m/s, corresponding to a Mach number of $Ma \approx 0.052$, in a direction parallel to the resonator. The reference length for this problem is assumed to be the distance between the inlet and the leading edge, regarding to the free propagation length of the jet. The fluid is considered a perfect gas $\rho = p/(RT)$. The simulation lasts for 100 ms, time enough to skip the initial transient of the flow and study the interested data to validate the results.
With this values the Reynolds number is estimated as $Re = Ul/\nu \approx 6470$ and a Prandtl number of $Pr = 0.72$. For the considered regime, we expect a weak turbulence behaviour. The vortex shedding frequency in the mouth region is caused by the oscillations of the jet. The hypothesis is that the vortex shedding frequency will synchronise with the frequency fixed by the resonator that corresponds to the fundamental frequency of the operating organ pipe, namely $f = 700$ Hz. The Strouhal-number is estimated at $St = fl/U \approx 0.214$. Again, the problem is resolved using OpenFOAM, comparing the results with those obtained numerically and experimentally by Fischer *et al.* [13].

3.2.2 Numerical setup

With respect to the previous laminar case, a turbulence model is now employed. The model considered is a one equation eddy-viscosity model, that employs a balance equation to simulate the behaviour of k [19], as explained in Section 2.2. The employed time step is $\Delta t = 1 \cdot 10^{-7}$ s. The simulation is carried on using the solver `rhoPimpleFoam` (compressible, transient, pressure based) using the following numerical schemes:

- 2^{nd} order backward scheme for temporal discretization (BDF2).
- For the convective term, he combination scheme of the 2^{nd} order linear scheme and the 1^{st} order upwind scheme based on blending function was applied by the so called `filteredLinear2`. This scheme basically behaves as the 2^{nd} order linear scheme. However, when the flux difference in control volume exceeds the criterion, this scheme is automatically blended with the upwind scheme to suppress numerical oscillation [35].
- For the turbulence, the `limitedLinear` scheme was used, total variation diminishing schemes, which is bounded with a variation of the well-known Sweby limiter [36]. This scheme recovers to the 2^{nd} central difference scheme when the limiter equals 1, and reduces to the 1^{st} upwind scheme when the limiter equals 0 [37].
- Unbounded, 2^{nd} order, conservative linear scheme for the viscous term.

Computational domain The computational domain is contained in a rectangle of 260×180 mm, as seen in Figure 7a. The pipe is positioned 24 mm away from the bottom wall and 75 mm away from the right wall, with the resonator parallel to the latter. In Figure 7b a detailed view of the mouth of the pipe can be seen, with the air inlet highlighted in blue.

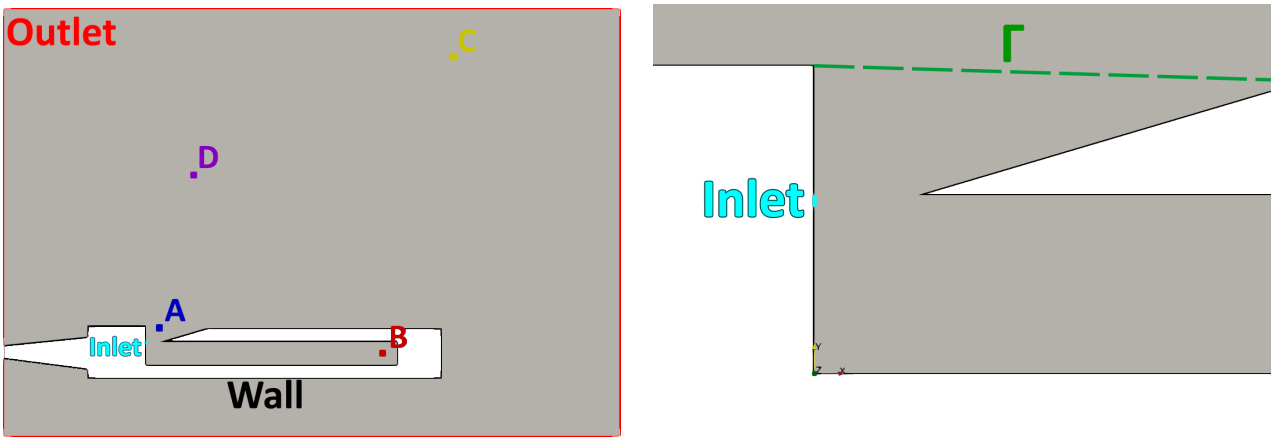

(a) (b)

Figure 7: Two-dimensional computational domain of the organ pipe and detail of the mouth area. Figure 7a shows the inlet (light blue), the walls of the pipe (black), and the outlet (red). Figure 7b has represented the averaging line Γ.

Boundary conditions Table 3 contains the boundary conditions chosen for the computational experiment. In Figures 7a and 7b the boundaries of the domain are highlighted. In particular, all the outside walls form

the outlet of the flow, highlighted on red on Figure 7a. The walls of the organ pipe are coloured black on both images. Lastly, the inlet is highlighted in blue, better seen in Figure 7b. For the pressure, the inlet and the organ pipe are defined as Neumann-like boundary conditions, and non-reflective boundary conditions for the outlet. The velocity, the temperature, and the turbulent kinetic energy have Dirichlet boundary conditions for both the inlet and the organ pipe walls, and a mix of Dirichlet-like and Neumann-like for the outlet. The turbulent kinematic viscosity and the turbulent thermal diffusivity have Neumann-like boundary conditions for the three boundaries.

	Inlet	**Outlet**	**Wall**
p	`zeroGradient`	`waveTransmissive`	`zeroGradient`
U	`fixedValue`	`inletOutlet`	`fixedValue`
T	`fixedValue`	`inletOutlet`	`fixedValue`
k	`fixedValue`	`inletOutlet`	`fixedValue`
ν_t	`zeroGradient`	`zeroGradient`	`zeroGradient`

Table 3: Boundary conditions for the two-dimensional organ pipe.

Mesh The computational domain previously explained was meshed using a total of 1.26×10^5 cells, seen in whole in Figure 8a. Near the mouth area and near the leading edge of the resonator is where the smallest cells can be found, with sizes $\Delta y = 1.5 \cdot 10^{-5}$ m. On a turbulent flow is important to estimate the Kolmogorov microscales to evaluate the grid size and computational time step in this case the Kolmogorov microscale $\eta = (\nu^3/\epsilon)^{1/4}$ m, with $\epsilon \sim U^3/l$, result in a $\eta \approx 7.6 \cdot 10^{-6}$. Compared with this, the grid size is way too large, and therefore the small turbulent structures cannot be resolved and have to be modelled, rising the need for the correct LES model.

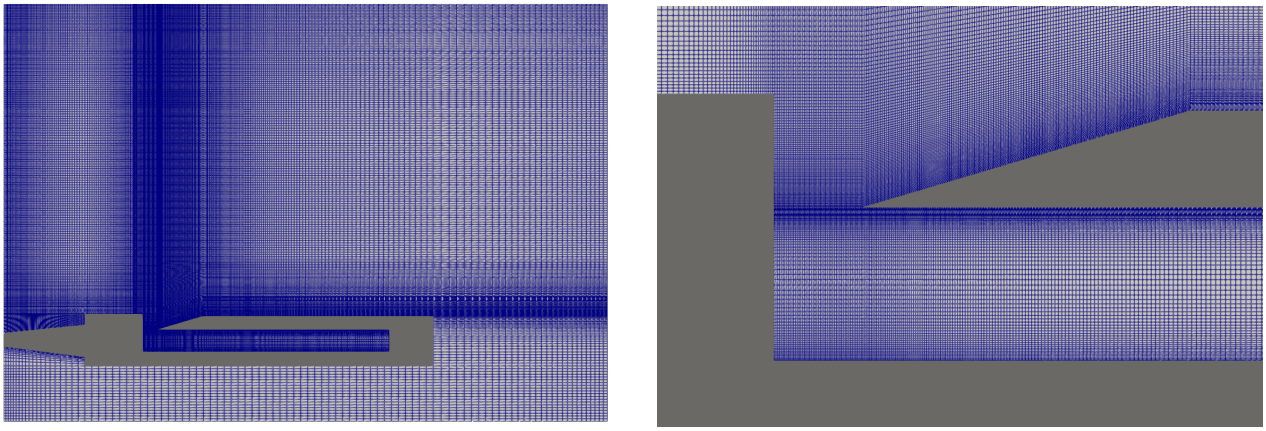

(a) (b)

Figure 8: Two-dimensional computational mesh of the organ pipe and detail of the mouth area.

3.2.3 Results of the standard case

Before starting to comment the obtained results, the sound mechanism of an organ pipe is described. In particular, we focus on two different sound generation mechanisms [38].

- **Edge tone**. The jet of air impinges against the leading edge of the organ pipe and generates vortices (Figure 11a), which create the sound defined as the edge tone.
- **Pipe tone**. The air column inside the pipe is periodically vibrating due to the jet's impulse and their interaction (Figures 10a to 10i). The pipe tone is then defined as the acoustic resonance that turns small pressure perturbations into periodic oscillations with large amplitudes.

The edge tone sound is weaker and shorter in duration than the pipe tone. The edge tone jet initiates the subsequent pipe tone and pairs with it to produce a louder, more harmonically rich, and more stable audible sound. For flue instruments like the one described in this project, with an attached pipe resonator, there are two feedback mechanisms acting on the oscillating jet of air leaving the inlet.

- **Hydrodynamic feedback**. The jet collides with the leading edge of the pipe, forming a dipole-type acoustic source, since most of the noise is inducec by the force fluctuations on the leading edge. The

fluctuating stream is parted by the leading edge, breaking into asymmetric vortex sheets, growing larger on both sides of the leading edge. The obstruction of the flow that the solid boundary creates changes the velocity and the pressure of the air around it. Fluid particles with lower velocity, and therefore higher pressure, will move towards those particles with smaller pressure, resulting in collisions between vortices. The frequency of the audible edge tone is about equal to the frequency of a selected particle of the vortices that pass through one side of the edge. This sound creates a very small perturbation on the jet, creating the fluctuations that start again the hydrodynamic feedback loop.

On Figure 9a the turbulent kinetic energy k can be seen on the final instant of the simulation, representing the increased turbulent flow due to the oscillating jet and the vortex sheets that form the hydrodynamic feedback loop.

- **Acoustic feedback**. The fluctuating edge tone helps the growing of the vortices introducing vorticity through the shear layer. Before the increasing pressure is sufficient to excite the resonance of the pipe, the oscillation frequency of the edge tone is lowered until it reaches the frequency of the normal modes of the pipe. The vortices that the leading edge sheds travel down the pipe, which leads to a complicated flow disturbance that either gives to or gets energy from the resonant acoustic field within the pipe. Simultaneously this perturbation interacts with the beginning of the pipe and affects the creation of new vortices in the shear layer, closing the acoustic feedback loop.

The complex flow formed due to the existence of a vortex sheet travelling down the resonator can be visualised on Figure 9a, whereas Figure 9b show the tendency that vortices have to travel towards the end of the pipe.is this complex flow that interacts with the acoustic field presented on Figures 10a to 10i.

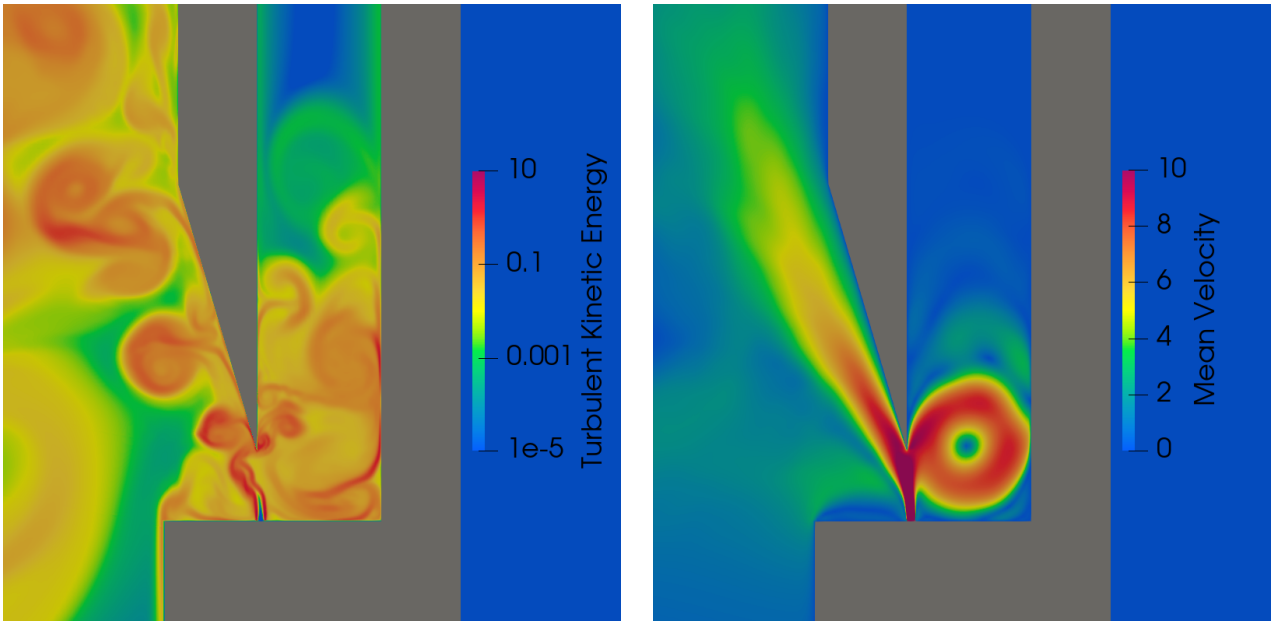

(a) (b)

Figure 9: Turbulent kinetic energy (m^2/s^2) and mean velocity at $t = 100$ ms, visualised on a logarithmic scale.

The first stages of the flow are defined by the displacement of the initial perturbation across the domain, as pictured on Figures 10a to 10i, where the perturbation wave can be seen travelling through the colour-coded pressure field. On the open air the sound wave propagates in a circular shape, expanding consistently in all directions. Meanwhile, it travels linearly over the resonator with a velocity of ~ 341 m/s, consisting on a planar wave front followed by the wall reflections, marked in red and yellows that signal its high pressure values. The sound wave propagates until it reaches the end of the resonator, where it gets reflected and travels back to the mouth (Figures 10c to 10e). When this wave returns to the mouth, it is reflected back into the resonator and starts the propagation of another circular wave front into the free space (Figures 10g to 10i).

On Figures 11a and 11b the final instantaneous velocity and its mean value are shown, respectively. In the first one the oscillating jet impacts with the resonator's leading edge, creating vortices in the free space and at the entrance of the resonator. Meanwhile, the mean velocity shows the average direction of the jet splitting over the edge, forming a strong vortex on the beginning part of the resonator.

To validate the methodology used to develop this part of the thesis, a comparison was made with the results obtained by Fischer *et al.* [12, 13], as it is the source of the geometry of the organ pipe. To get consistent results

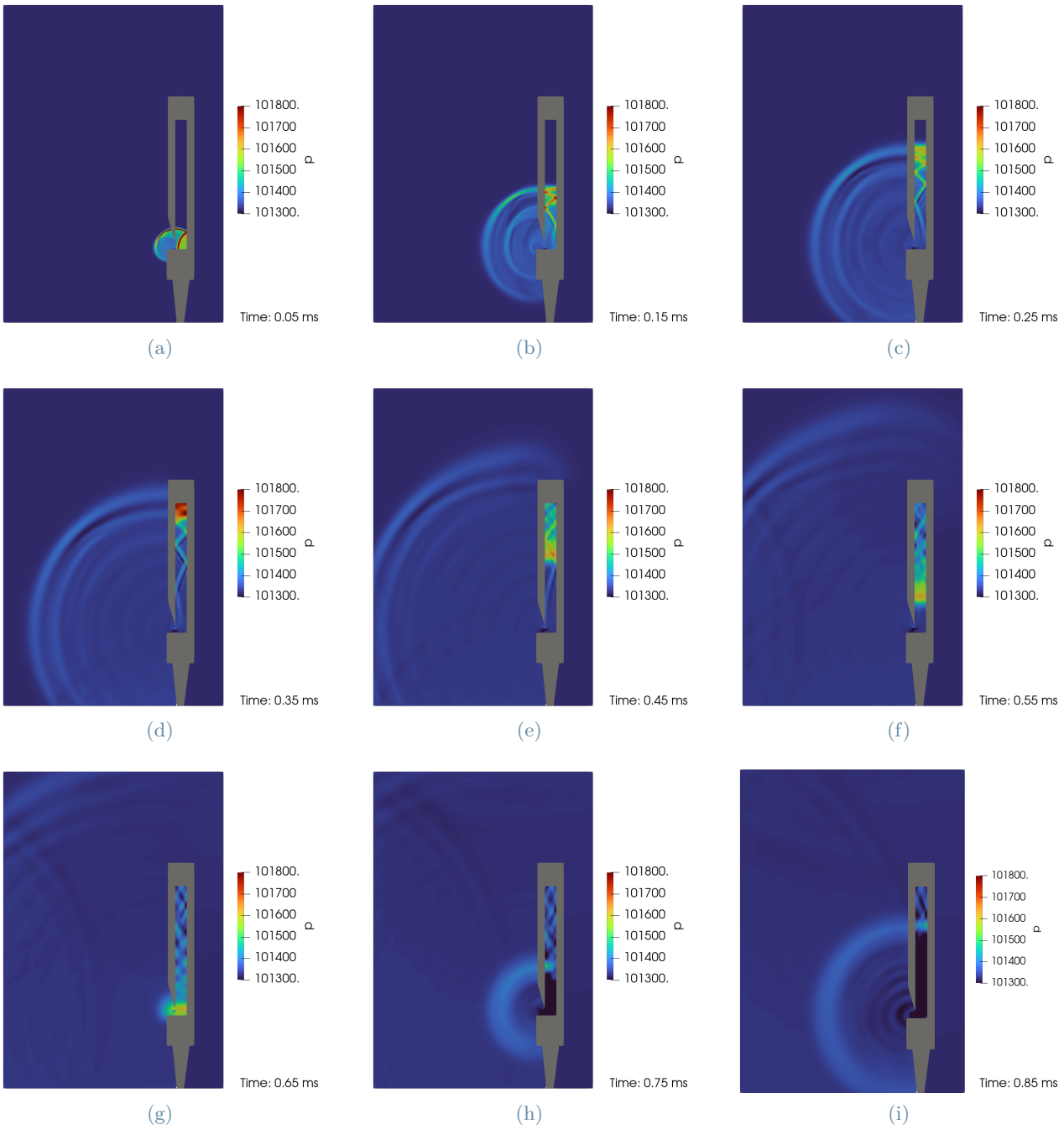

Figure 10: Sequence of a numerical simulation of an operating stopped wooden organ pipe, from 0.05 ms to 0.85 ms. The pressure initial perturbation is shown through the pressure (Pa) field.

with the reference, the same methodology was used. The physical quantities of relevance in this case were both two-dimensional components of the velocity of the flow, V_X and V_Y, and the pressure. The reference axis are those represented in Figure 7b. The sample sets were spatially averaged over Γ, as seen in Figure 7b, a spatial expansion of 27.2 mm divided in 300 points, sampling the data with a time-step of $\Delta t = 0.1$ ms.
Figure 12 pictures the time evolution of the mean velocity components obtained through this method, compared to those obtained by the reference. V_Y, almost perpendicular to Γ, has a strong periodicity, matching the theoretical 700 Hz expected from the organ pipe.V_X, parallel to the direction of the incoming jet carries the flow velocity with its high fluctuations in amplitude, whereas V_Y is more stable in frequency, carrying the acoustic field. It is in the latter where the influence of the interaction between the fluctuating jet and the strong periodicity of the acoustic field inside the pipe is shown.
The similarity between both results is evident, with similar behaviours in both velocity components, with only a small divergence in their respective mean values: $\langle V_Y \rangle$ has a 3% difference and the more chaotic $\langle V_X \rangle$ has a 8%.

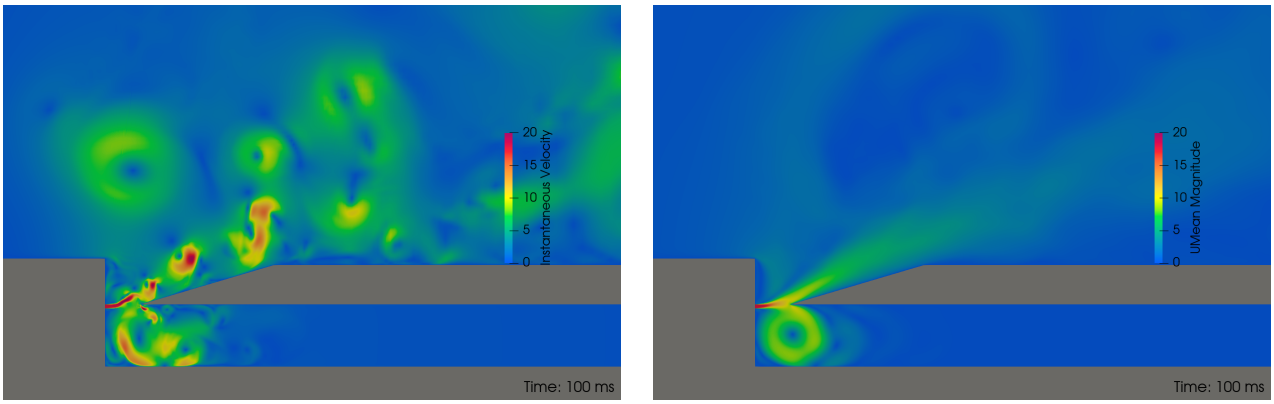

(a) (b)

Figure 11: Instantaneous and mean velocity (m/s) at $t = 100$ ms.

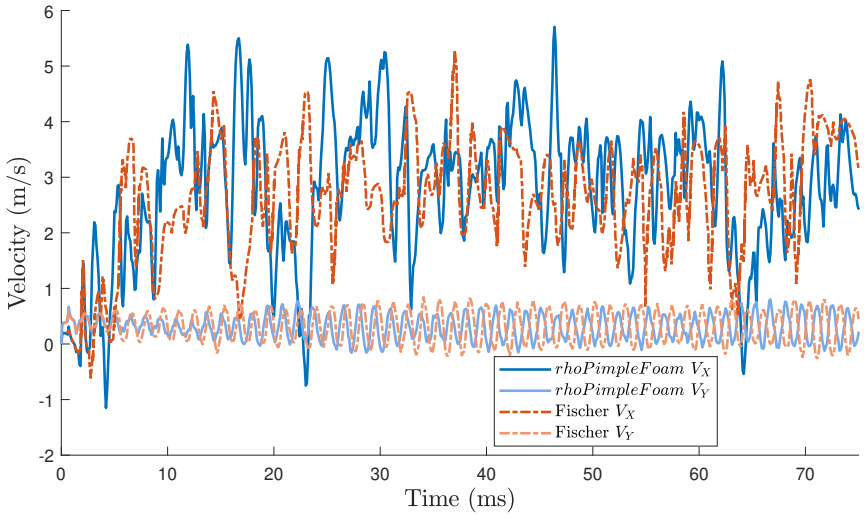

Figure 12: Mean velocity signals obtained over Γ, compared to those obtained from the reference.

The SPL-spectrum recorded over Γ is represented in Figure 13, compared with experimental data obtained by Fischer *et al.* [13]. Labelled are the peaks of the acoustic pipe mode frequencies (1^{st}, 3^{rd} and 5^{th}), but also the even (2^{nd}, 4^{th} and 6^{th}) harmonics for the closed end pipe.
The deviation of the experimental data is only of 5% in frequency, which is considered a good result taking into account the averaged values used and the short simulation time. The experimental data was obtained using a microphone located at 0.5 m from the mouth area, which explains the difference in the values of the amplitude. It should also be considered that a two-dimensional simulation is not expected to perfectly represent a real three-dimensional case.
Finally, a computation of the fluctuating pressure outside of the computational domain using the FWH acoustic analogy was also performed. Figure 14b pictures the non-dimensional fluctuating pressure obtained both on a probe in the far field inside the computational domain, and through the FWH acoustic analogy on an observer located outside the computational domain. Figure 14a shows the SPL obtained through both methods. Again, the FHW observer registers a lower amplitude with respect to the far field probe because it is positioned further away from the mouth of the instrument. The shape of the SPL is similar between both results, with similar valleys and peaks, with a more notable peak on the second harmonic ($\sim$ 1400 Hz) on the FWH observer compared with the probe.

3.2.4 Modified geometries

Following the study and validation of the standard geometry, another set of simulations were performed modifying the geometry of the organ pipe. The scope of this section is to observe the change in behaviour of the aeroacoustic flow when changing the distance between the leading edge and the inlet jet.

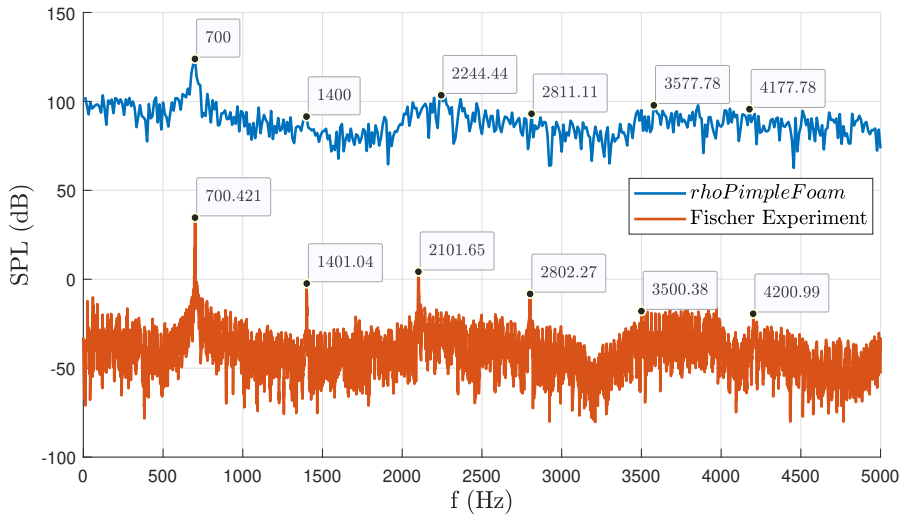

Figure 13: SPL of the two-dimensional organ pipe over Γ. The experimental data was shifed by −100 dB by Fischer *et al.* [13].

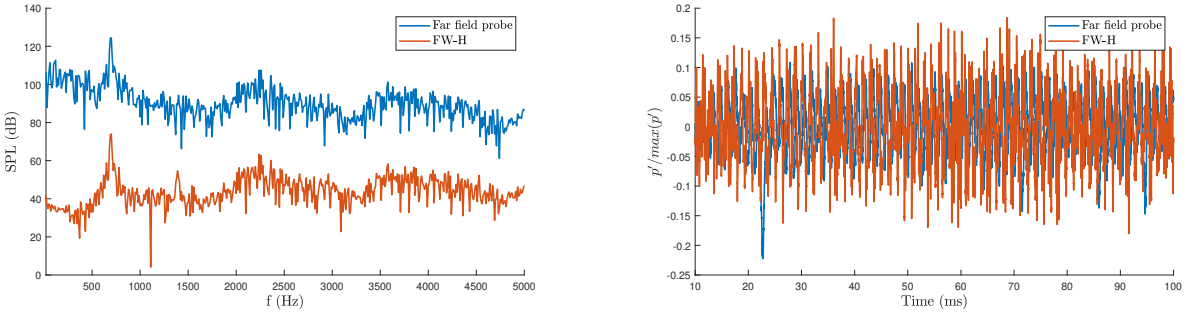

(a) (b)

Figure 14: Comparison of the SPL and the non-dimensional fluctuating pressure obtained from the computational experiment and through the FWH acoustic analogy.

Mesh The different geometries studied were created by moving the leading edge of the resonator. Figure 15 shows the different configurations studied: in blue, the reference position of the organ pipe. Red marks the geometry of the close edge. The next considered edge is marked in yellow, indicated as far edge. Finally, purple marks the furthest edge geometry.
Table 4 gathers the main difference from the change in geometry: the distance d between the inlet and the edge and the number of cells that compose the mesh. The flow specifications and the rest of the numerical parameters stay the same in all the cases.

	d	**Number of cells**
Standard edge	5.5 mm	1.26×10^5
Close edge	3.0 mm	1.22445×10^5
Far edge	10.0 mm	1.31895×10^5
Furthest edge	15.0 mm	1.39005×10^5

Table 4: Difference in geometry between the cases.

Results For these cases the results were analysed using different probes located over the domain, see Figure 7a. Probe A is positioned near the area of the mouth of the pipe. Probe B is towards the end of the resonator. Probes C and D are positioned in the middle of the flow, with probe C having the biggest distance from the mouth.

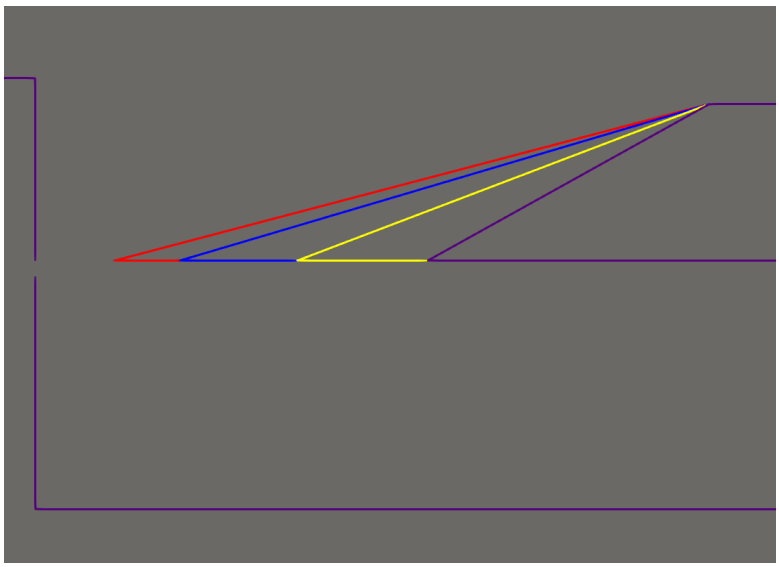

Figure 15: Leading edge positioning for the different geometries.

The time history of the obtained pressures is shown in Figure 16. For all cases the amplitude recorded by the probes follows the same logic. Probe B is the one that records the highest pressure amplitudes, being positioned in the resonator. The other probes' pressure amplitude decreases as they are put far away from the mouth. The close edge case is the case with the highest and more chaotic pressure values near the mouth area, as the closer the leading edge is to the inlet, the more and more intense vortices are created. The further away the leading edge is from the inlet, the more pressure is captured by the probes. Less and weaker vortices are formed, and a weaker sound wave is propagating on the resonator.

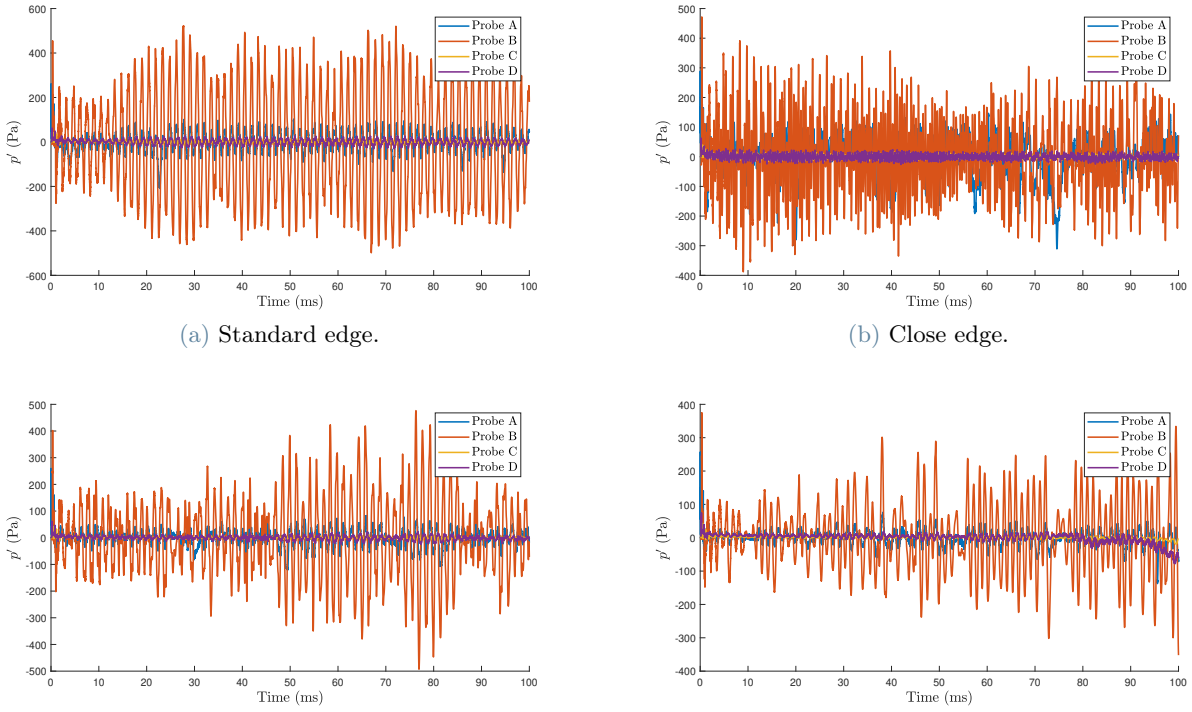

(a) Standard edge.

(b) Close edge.

(c) Far edge.

(d) Furthest edge.

Figure 16: Fluctuating pressure history for probes A, B, C, D for the different problem configurations.

Figure 17 shows the SPL-spectrum of the different leading edge configurations. Compared to the standard configuration, the close leading edge has the first harmonic on a lower frequency. Moving the edge closer to the inlet, makes the actual length of the resonator longer, and therefore the frequency of the first harmonic is the smaller of all the configurations. Conversely, when the position of the leading edge is pushed away from the

inlet, the resonator is effectively shorter and therefore register a higher frequency for the first harmonic.
Another behaviour of organ pipes can be found here. Similar to the edge tone (first hydrodynamic mode), for lower values of the jet velocity there is a proportional relation between itself and the frequency of produced by the instrument. When the latter reaches the value of the fundamental frequency of the pipe, synchronisation happens. The value of the recorded frequency is locked to the this fundamental frequency until the edge tone frequency is close to the third harmonic, and as closed pipes only develop odd harmonics it works as the second acoustic pipe mode frequency. This second synchronisation causes a jump in the registered frequency to the second resonance [14].
This phenomenon happens on the organ pipe configuration with the close leading edge of the resonator. As the edge is closer, the second acoustic pipe mode is reached with a lower jet velocity than the standard case. For this reason, on Figure 17 it can be seen how the dominant frequency for the close edge case is the third harmonic.

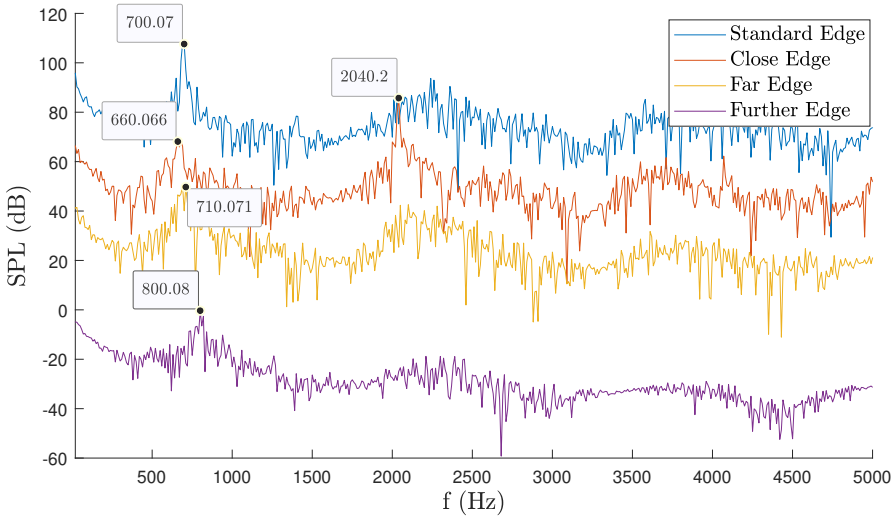

Figure 17: Comparison of the SPL of probe C for the different edges. The results for the modified geometries have offsets of −25 dB for the close edge, −50 dB for the far edge, and −100 dB for the furthest edge.

3.3. Three-dimensional

In this section the results of the three-dimensional simulation are shown and commented. Being LES turbulence model designed for three-dimensional problems, the results are expected to have a significant variation with respect of the two-dimensional case.

3.3.1 Flow specifications

In Figure 18 the whole three-dimensional model of the organ pipe can be seen. For the flow, a static flow with an initial pressure of $p_0 = 101325$ Pa, a temperature of $T_0 = 293$ K, a kinematic viscosity of $\nu = 1.53 \cdot 10^{-5}$ m^2/s, and a jet velocity of 18 m/s. The fluid is considered a perfect gas $\rho = p/(RT)$. The simulation is also set to last for 100 ms.

Figure 18: Three-dimensional representation of the organ pipe tube.

As the geometry and the domain were created using the `blockMesh` utility of OpenFOAM [21], a slight change in the geometry of the edge had to be done, as seen on Figure 19, where this part of the organ pipe is see, in

red for the three-dimensional geometry and in blue for the two-dimensional case. This change was done to be able to create the mesh properly without the use of non-hexahedrical cells.

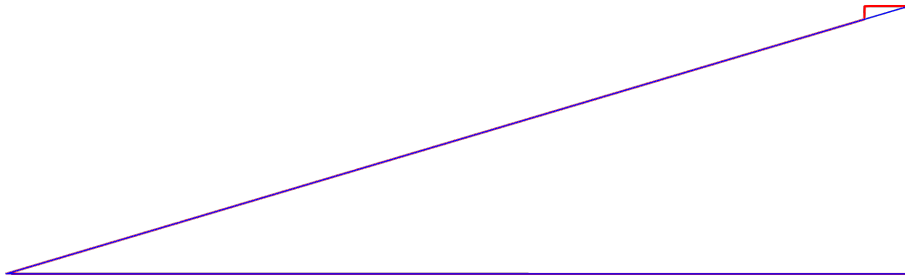

Figure 19: Difference in the geometry of the edge between the two-dimensional and three-dimensional case.

3.3.2 Numerical Setup

The following numerical schemes are set for the three-dimensional case.

- 2^{nd} order backward scheme for temporal discretization.
- 2^{nd} order unbounded limited, namely `filteredLinear2` in OpenFOAM, for the convective term and $1^{\text{st}}/2^{\text{nd}}$ order unbounded `limitedLinear` for the turbulence.
- Unbounded, 2^{nd} order, conservative linear scheme for the viscous term.

Computational domain In Figure 20 is the computational domain is shown.The external domain is contained in a prism of $125 \times 36.5 \times 51.5$ mm. This box extends through all the length of the organ pipe, 15 mm over it, and extends for another 15 mm over each lateral.

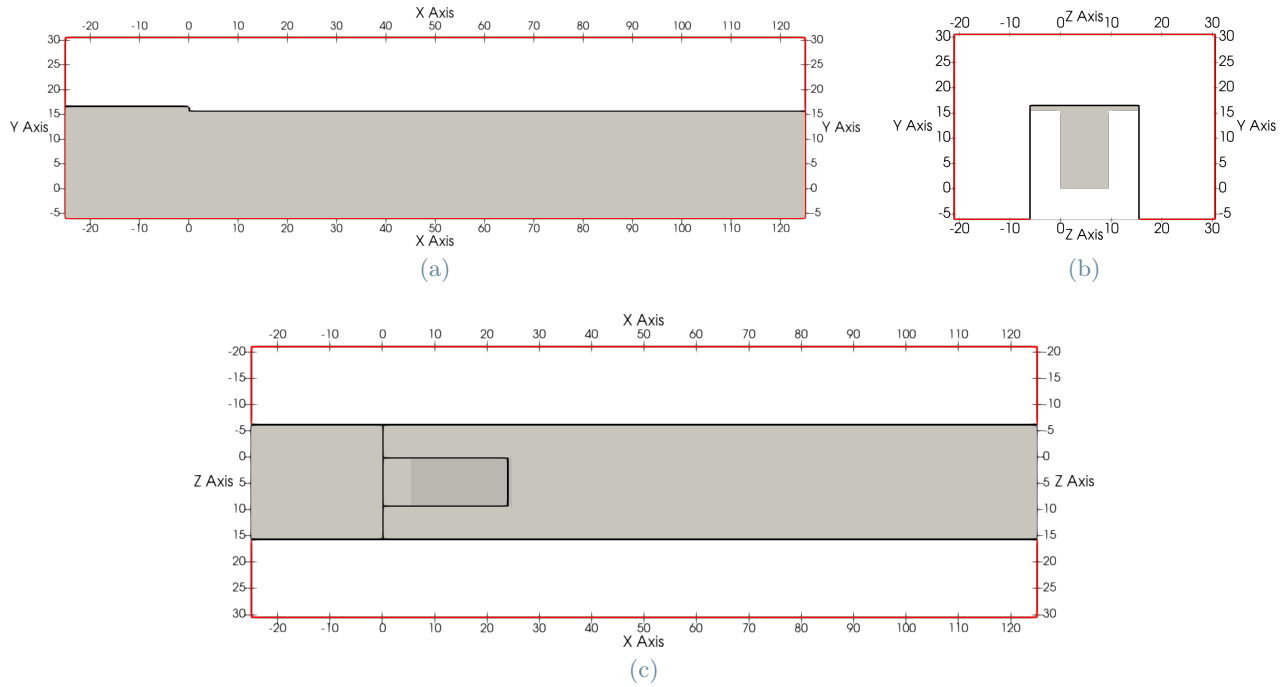

Figure 20: Computational domain of the three-dimensional computational experiment of the organ pipe.

Boundary conditions Following the same logic previously stated, the boundary conditions are the same of the two-dimensional case, contained on Table 3. The new boundaries that appear on the domain after adding

the third dimension to the experiment follow the same logic as for the previous case, where the walls of the organ pipe follow the `Wall` boundary condition and the external boundaries are considered `Outlet`.

Mesh The mesh, seen in Figures 21a to 21d for the three-dimensional case is created using the two-dimensional case as a reference. The centre of the mesh, which covers the entirety of the resonator, is an extension of the two-dimensional case. The rest of the mesh extends from here, following the rest of the geometry of the instrument and covering the whole computational domain. For this, a total of 6.4416×10^6 cells where employed, more than 50 times those used for the previous case. Similarly to Section 3.2.2, turbulence modelling is required, as the minimum cell size is of $\Delta y = 1.5 \cdot 10^{-5}$ m, bigger than the Kolmogorov microscales.

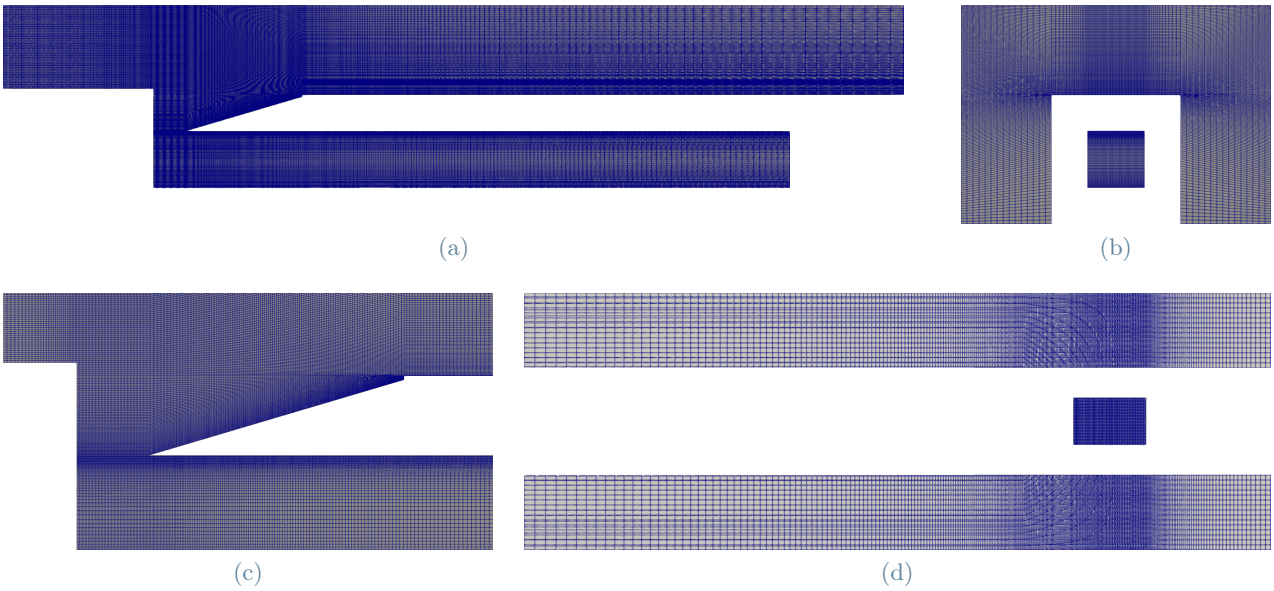

Figure 21: Mesh of the three-dimensional computational domain from different perspectives.

3.3.3 Results

The main drawback of performing a computational three-dimensional experiment is the increased computational cost with respect to the two-dimensional case. In this case, the three-dimensional computational domain is shorter than its two dimensional counterpart in both the x and y directions. Nevertheless, adding the z axis causes a total increase of the total number of cells by a factor of 50. The numerical simulations were calculated in parallel on the computational cluster of the Department of Mechanical Engineering of Politecnico di Milano, using 4 computational cores for the two-dimensional case and 40 cores for the three-dimensional case. As a result, the time needed to computationally simulate the 100 ms of each case goes from approximately 28 hours in the two-dimensional case, to over 31 days on the three-dimensional case.
The initial perturbation expansion is again shown, in Figures 22a to 22i in a two-dimensional way, showing the pressure field of a slice of the xy plane of the computational domain passing through the middle of the resonator, and again in Figures 23a to 23i through pressure contours. The same behaviour explained on Section 3.2.3 can be seen here, with the acoustic wave travelling on the resonator with a planar front and propagating as a spherical wave on the free space, as seen in Figure 23a. The speed of propagation can be estimated from this images as ~ 341 m/s. It is worth mentioning that this simulation is influenced by the relatively small size of the computational domain, as some weak reflections caused by the boundaries can be seen on Figure 22b. The pressure wave registers a lower pressure with respect to the two-dimensional case, as turbulent dissipation is stronger on three-dimensional cases.
Figure 24 shows the time history of the pressure obtained by probe A (positioned as seen in Figure 7a). The three-dimensional case shows a smaller amplitude for the pressure, but more stable oscillation. Due to turbulence being mainly a three-dimensional effect, in two-dimensional cases, vortex structures are more robust and rolled up eddies survive longer than in three-dimensional cases.

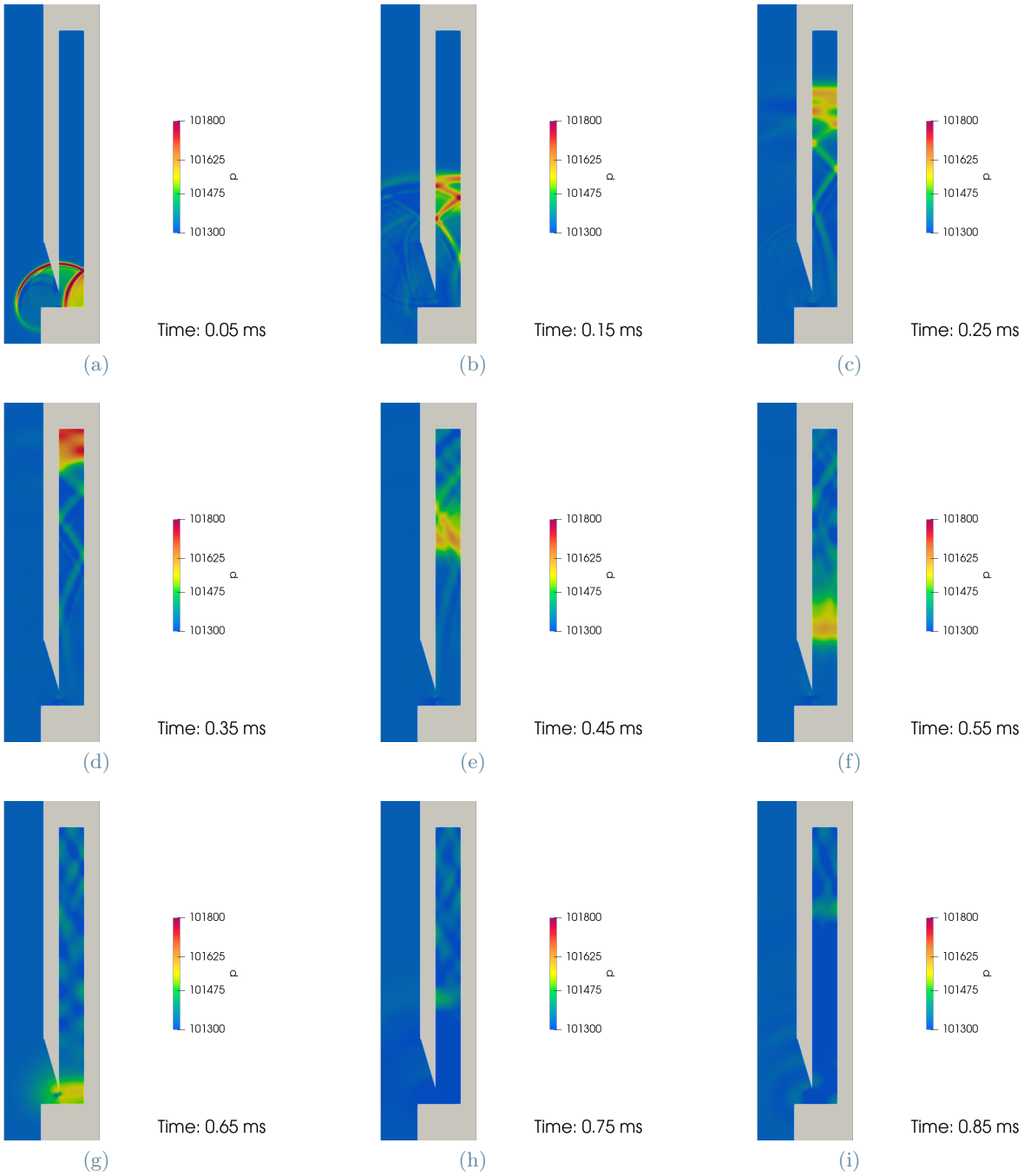

Figure 22: Sample plane of the numerical three-dimensional simulation of an operating stopped wooden organ pipe, from 0.05 ms to 0.85 ms. The plane shown here coincides with the centre of the organ pipe ($z = 4.75$ mm)

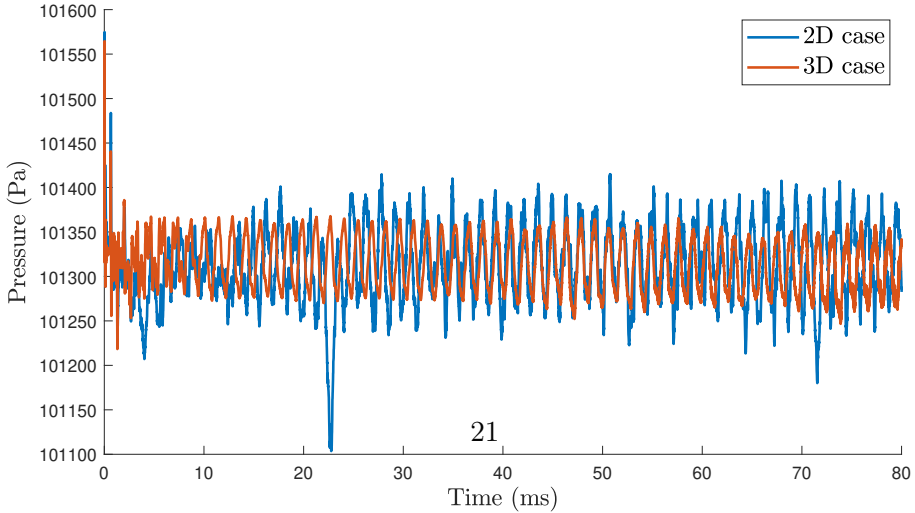

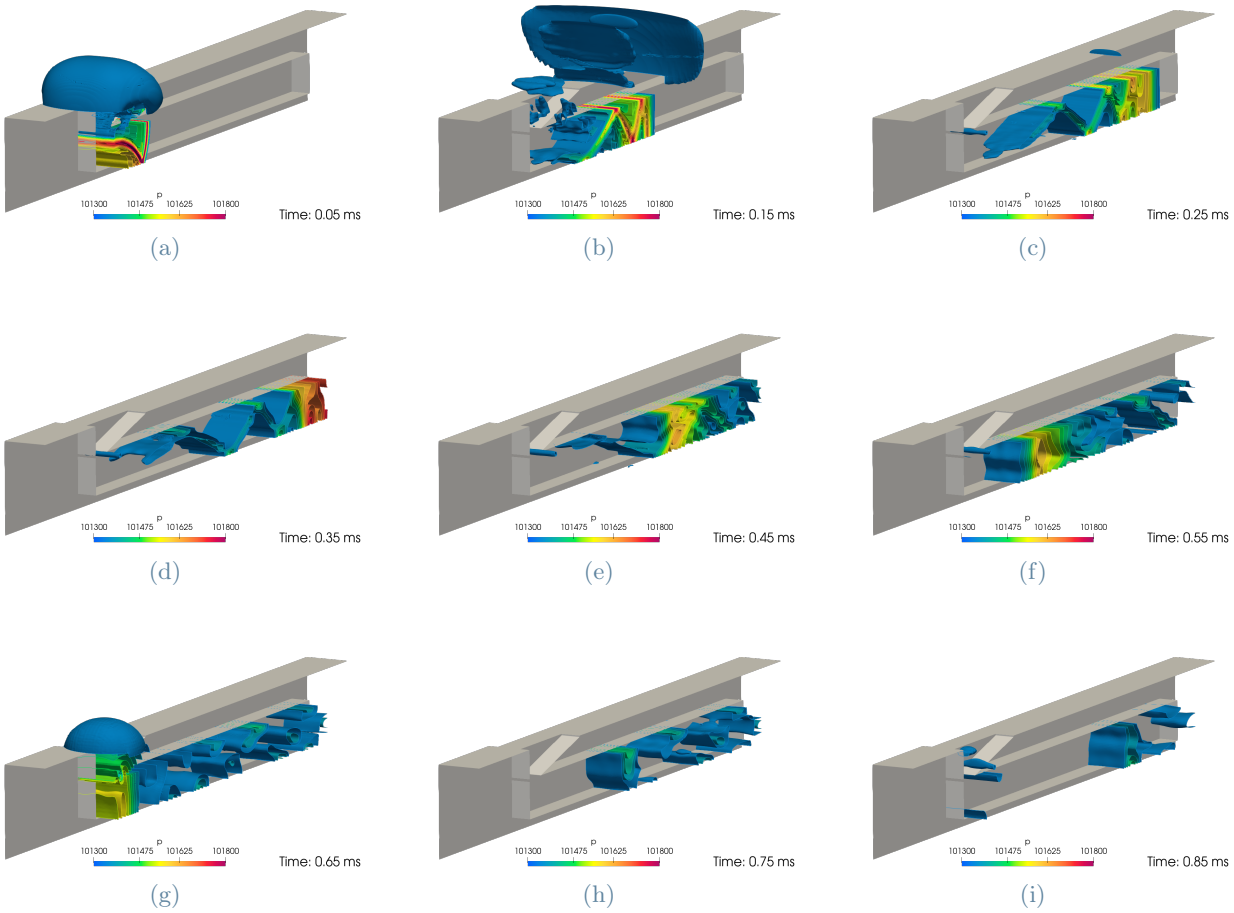

Figure 23: Three-dimensional sequence of the three-dimensional model of an operating stopped wooden organ pipe, from 0.05 ms to 0.85 ms.

Figures 25a and 25b show respectively the mean velocity field obtained from the two-dimensional and three-dimensional models. In this images the difference in strength between the velocity field clearly show that robustness that the two-dimensional case shows on the vortex line situated at the beginning of the resonator against the three-dimensional case.

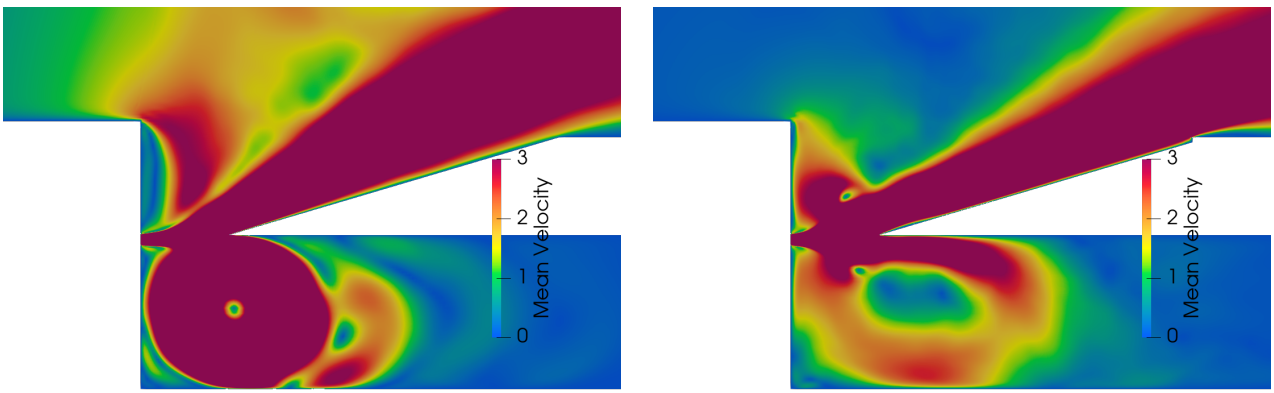

(a) Two-dimensional (b) Three-dimensional

Figure 25: Mean velocities (m/s) at $t = 100$ ms for both the two-dimensional and three-dimensional cases.

Figure 26 shows the SPL obtained on the same probe. For every harmonic, but more specifically for the first one (the one located at 700 Hz) the SPL value is almost identical. For the rest of the spectra, the three-dimensional model registers lower dB. Being this case more stable than the two-dimensional case, the peaks relative to the different harmonics (the 1^{st}, 3^{rd} and 5^{th} that are the natural harmonics of the closed organ pipe, but also the 2^{nd}, 4^{th} and 6^{th}) are more notable.

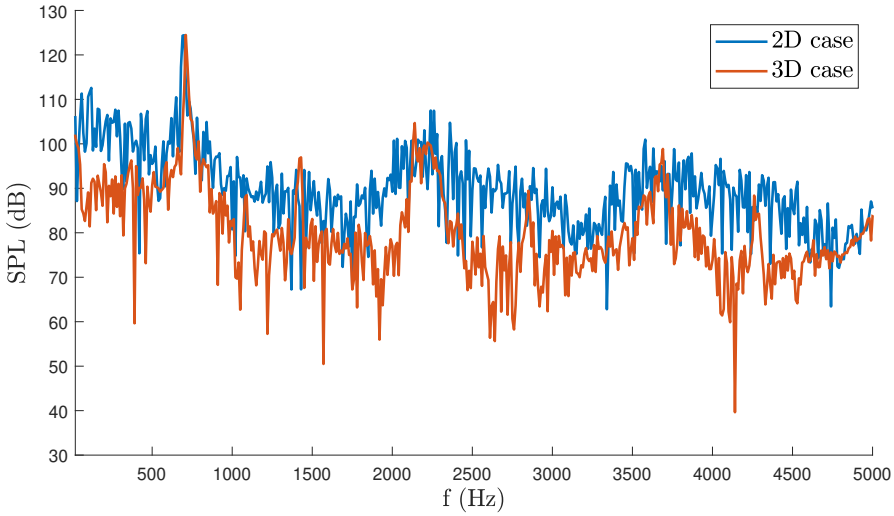

Figure 26: SPL obtained from probe A in both organ pipe cases.

Due to the high computational cost of the three-dimensional simulation, only the last 28.7 ms of simulation were able to be used to calculate the far field acoustic data through the FWH acoustic analogy. Figure 27 shows the obtained results and plots them together with the experimental results of Fischer *et al.* [13]. Even with a visible difference in shape due to the difference on values taken, the FWH aeroacoustic analogy captures correctly the shape of the SPL, with the higher peak situated at the corresponding 700 Hz of the first harmonic, with the rest of the peaks greatly defined.

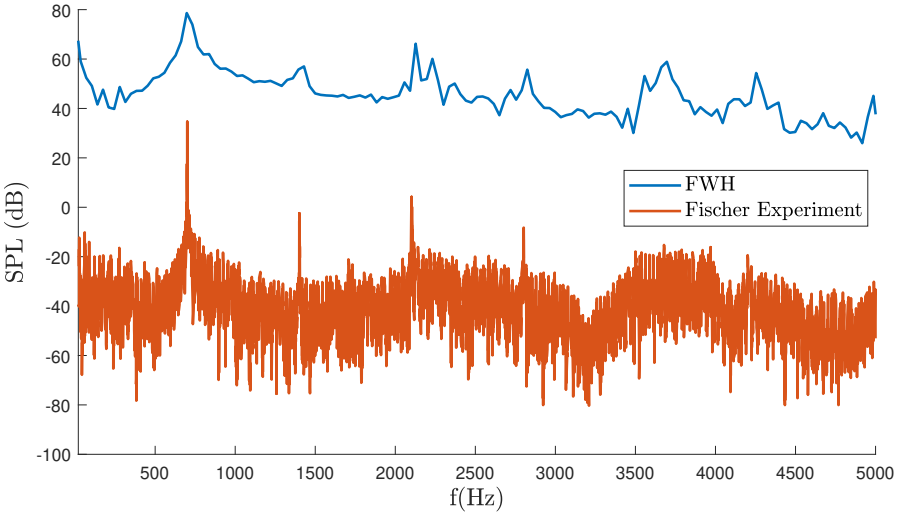

Figure 27: Comparison between the SPL of the far field of the three-dimensional case and Fischer *et al.* experiment [13]. The experimental data was shifed by -100 dB by Fischer *et al.*.

4. Conclusions

The main result of this study is the use of the FWH aeroacoustic analogy over a LES simulation of the flow caused by a three-dimensional model of an organ pipe, using the OpenFOAM C++ toolbox to create and perform the CFD simulation of the flow.

First, the noise induced by a squared cylinder was considered, The obtained results helped validating the methodology and understanding the behaviour of the acoustic field. The compressible and laminar simulation well reproduce the aerodynamic forces that cause the aeolian tones, as seen in Table 2, and the acoustic field, proven through the directivities plot in Figure 6.
Next, a two-dimensional model of an organ pipe is considered. The flow is modelled via LES and the results follow well the expected behaviour for the generation of sound, as seen in Figures 9a and 9b. In Figure 12 there is a comparison between the model and the reference is made, obtaining not only a validation and the knowledge that the acoustic field is carried on the exiting component of the velocity. The acoustics have also a good representation on this model, obtained both directly from the flow field and through the FWH acoustic analogy. It was also proven that the obtained acoustic from the two-dimensional model behave correctly on changes of geometry.
Finally, the three-dimensional model shows similar results as the two-dimensional case. Differences are present due to the nature of the two-dimensional flow and the effects of turbulence. Regardless, the three-dimensional case is more stable and capture betters the acoustics both through the flow field and through the FWH acoustic analogy. Nevertheless, the high computational cost of the three-dimensional simulation with respect the two-dimensional model do not compensate the quality of in the results.
The use of the FWH analogy is validated, getting booth result for the acoustic pressure outside the computational domain. Both in the two-dimensional an three-dimensional models, its use provides good understanding on both the harmonics and in the amplitude.

References

[1] Michael James Lighthill and Maxwell Herman Alexander Newman. On sound generated aerodynamically I. General theory. *Proceedings of the Royal Society of London. Series A. Mathematical and Physical Sciences*, 211(1107):564–587, 1952. doi: 10.1098/rspa.1952.0060. URL `https://royalsocietypublishing.org/doi/abs/10.1098/rspa.1952.0060`.

[2] Michael James Lighthill. On sound generated aerodynamically II. Turbulence as a source of sound. *Proceedings of the Royal Society of London. Series A. Mathematical and Physical Sciences*, 222(1148):1–32, 1954. doi: 10.1098/rspa.1954.0049. URL `https://royalsocietypublishing.org/doi/abs/10.1098/rspa.1954.0049`.

[3] N. Curle and Michael James Lighthill. The influence of solid boundaries upon aerodynamic sound. *Proceedings of the Royal Society of London. Series A. Mathematical and Physical Sciences*, 231(1187):505–514, 1955. doi: 10.1098/rspa.1955.0191. URL `https://royalsocietypublishing.org/doi/abs/10.1098/rspa.1955.0191`.

[4] J. E. Ffowcs Williams, D. L. Hawkings, and Michael James Lighthill. Sound generation by turbulence and surfaces in arbitrary motion. *Philosophical Transactions of the Royal Society of London. Series A, Mathematical and Physical Sciences*, 264(1151):321–342, 1969. doi: 10.1098/rsta.1969.0031. URL `https://royalsocietypublishing.org/doi/abs/10.1098/rsta.1969.0031`.

[5] A Hirschberg, Jean Kergomard, and Gabriel Weinreich. *Mechanics of Musical Instruments*, chapter 7, pages 291–369. Springer, January 1995.

[6] Benoit Fabre, Joël Gilbert, Avraham Hirschberg, and Xavier Pelorson. Aeroacoustics of musical instruments. *Annual Review of Fluid Mechanics*, 44(1):1–25, 2012. doi: 10.1146/annurev-fluid-120710-101031. URL `https://doi.org/10.1146/annurev-fluid-120710-101031`.

[7] N.H. Fletcher and T. Rossing. *The Physics of Musical Instruments*. Springer New York, 2008. ISBN 9780387983745. URL `https://books.google.es/books?id=9CRSRYQlRLkC`.

[8] John W. Coltman. Sounding mechanism of the flute and organ pipe. *The Journal of the Acoustical Society of America*, 44(4):983–992, 1968. doi: 10.1121/1.1911240. URL `https://doi.org/10.1121/1.1911240`.

[9] John W. Coltman. Sound radiation from the mouth of an organ pipe. *The Journal of the Acoustical Society of America*, 46(2B):477–477, 1969. doi: 10.1121/1.1911717. URL `https://doi.org/10.1121/1.1911717`.

[10] John W. Coltman. Jet drive mechanisms in edge tones and organ pipes. *The Journal of the Acoustical Society of America*, 60(3):725–733, 1976. doi: 10.1121/1.381120. URL `https://doi.org/10.1121/1.381120`.

[11] Jost Fischer. *Nichtlineare Kopplungsmechanismen akustischer Oszillatoren am Beispiel der Synchronisation von Orgelpfeifen*. PhD thesis, Universität Potsdam, April 2014.

[12] Jost Leonhardt Fischer. *Feedback of Different Room Geometries on the Sound Generation and Sound Radiation of an Organ Pipe*, pages 109–142. Springer International Publishing, Cham, 2017. ISBN 978-3-319-47292-8. doi: 10.1007/978-3-319-47292-8_4. URL https://doi.org/10.1007/978-3-319-47292-8_4.

[13] Jost Leonhardt Fischer, Rolf Bader, and Markus Abel. On the dynamics of the flow and the sound field of an organ pipes's mouth region. *arXiv: Fluid Dynamics*, 2019. doi: 10.48550/ARXIV.1912.06484. URL https://arxiv.org/abs/1912.06484.

[14] Masataka Miyamoto, Yasunori Ito, Takuya Iwasaki, Takahiro Akamura, Kin'ya Takahashi, Toshiya Takami, Taizo Kobayashi, Akira Nishida, and Mutsumi Aoyagi. Numerical study on acoustic oscillations of 2D and 3D flue organ pipe like instruments with compressible LES. *Acta Acustica united with Acustica*, 93:154–171, January 2013. doi: 10.3813/AAA.918599.

[15] Taizo Kobayashi, Toshiya Takami, Masataka Miyamoto, Kin'ya Takahashi, Akira Nishida, and Mutsumi Aoyagi. 3D calculation with compressible LES for sound vibration of ocarina. *arXiv: Fluid Dynamics*, 2009. doi: 10.48550/ARXIV.0911.3567. URL https://arxiv.org/abs/0911.3567.

[16] Avraham Hirschberg and Sjoerd Rienstra. An introduction to aeroacoustics. *Eindhoven university of technology*, 1823:18–7, August 2004.

[17] Stephen B. Pope. *Turbulent Flows*. Cambridge University Press, 2000. doi: 10.1017/CBO9780511840531.

[18] J. Smagorinsky. General circulation experiments with the primitive equations: I. the basic experiment. *Monthly Weather Review*, 91(3):99 – 164, 1963. doi: 10.1175/1520-0493(1963)091<0099:GCEWTP>2.3.CO;2. URL https://journals.ametsoc.org/view/journals/mwre/91/3/1520-0493_1963_091_0099_gcewtp_2_3_co_2.xml.

[19] Akira Yoshizawa. Statistical theory for compressible turbulent shear flows, with the application to subgrid modeling. *The Physics of Fluids*, 29(7):2152–2164, 1986. doi: 10.1063/1.865552. URL https://aip.scitation.org/doi/abs/10.1063/1.865552.

[20] H.K. Versteeg and W. Malalasekera. *An Introduction to Computational Fluid Dynamics: The Finite Volume Method*. Pearson Education Limited, 2007. ISBN 9780131274983. URL https://books.google.es/books?id=RvBZ-UMpGzIC.

[21] OpenCFD Limited. The open source computational fluid dynamics (CFD) toolbox organization, 2004. URL https://www.openfoam.com/. Accessed: 2022-11-07.

[22] Hrvoje Jasak. *Error Analysis and Estimation for the Finite Volume Method With Applications to Fluid Flows*. PhD thesis, University of Cambridge, January 1996.

[23] Christopher Greenshields, Henry Weller, Luca Gasparini, and Jason Reese. Implementation of semi-discrete, non-staggered central schemes in a colocated, polyhedral, finite volume framework, for high-speed viscous flows. *International Journal for Numerical Methods in Fluids*, 63:1 – 21, 01 2009. doi: 10.1002/fld.2069.

[24] Tobias Holzmann. *Mathematics, Numerics, Derivations and OpenFOAM®*. Holzmann CFD, November 2019.

[25] T.J Poinsot and S.K Lelef. Boundary conditions for direct simulations of compressible viscous flows. *Journal of Computational Physics*, 101(1):104–129, 1992. ISSN 0021-9991. doi: https://doi.org/10.1016/0021-9991(92)90046-2. URL https://www.sciencedirect.com/science/article/pii/0021999192900462.

[26] F. Farassat. Derivation of formulations 1 and 1A of Farassat. Technical Report NASA/TM-2007-214853, NASA, March 2007.

[27] F. Farassat. Linear acoustic formulas for calculation of rotating blade noise. *AIAA Journal*, 19(9):1122–1130, 1981. doi: 10.2514/3.60051. URL https://doi.org/10.2514/3.60051.

[28] Kenneth S. Brentner. Prediction of helicopter discrete frequency rotor noise- a computer program incorporating realistic blade motions and advanced formulation. Technical Report NASA/TM-1986-87721, NASA, October 1986.

[29] Andrey Epikhin, Ilya Evdokimov, Matvey Kraposhin, Michael Kalugin, and Sergei Strijhak. Development of a dynamic library for computational aeroacoustics applications using the openfoam open source package. *Procedia Computer Science*, 66:150–157, 2015. ISSN 1877-0509. doi: https://doi.org/10.1016/j.procs.2015.11.018. URL https://www.sciencedirect.com/science/article/pii/S1877050915033670. 4th International Young Scientist Conference on Computational Science.

[30] O. Inoue, M. Mori, and N. Hatakeyama. Aeolian tones radiated from flow past two square cylinders in tandem. *Physics of Fluids*, 18(4):046101, 2006. doi: 10.1063/1.2187446. URL https://doi.org/10.1063/1.2187446.

[31] Mohamed Sukri Mat Ali, Con J. Doolan, and Vincent Wheatley. The sound generated by a square cylinder with a splitter plate at low reynolds number. *Journal of Sound and Vibration*, 330(15):3620–3635, 2011. ISSN 0022-460X. doi: https://doi.org/10.1016/j.jsv.2011.03.008. URL https://www.sciencedirect.com/science/article/pii/S0022460X1100188X.

[32] B. P. Leonard. Simple high-accuracy resolution program for convective modelling of discontinuities. *International Journal for Numerical Methods in Fluids*, 8(10):1291–1318, 1988. doi: https://doi.org/10.1002/fld.1650081013. URL https://onlinelibrary.wiley.com/doi/abs/10.1002/fld.1650081013.

[33] Luca Sorini. Studio numerico del modello aeroacustico di una canna d'organo labiale aperta. Master's thesis, Politecnico di Milano, 2022.

[34] Alexander Schuke Orgelbau GmbH, 2017. URL http://www.schuke.de/. Accessed: 2022-09-21.

[35] Takamasa Hasama, Toshihide Saka, Yoshiaki Itoh, Koji Kondo, Manabu Yamamoto, Tetsuro Tamura, and Mitsuo Yokokawa. Evaluation of aerodynamic instability for building using fluid–structure interaction analysis combined with multi-degree-of-freedom structure model and large-eddy simulation. *Journal of Wind Engineering and Industrial Aerodynamics*, 197:104052, 2020. ISSN 0167-6105. doi: https://doi.org/10.1016/j.jweia.2019.104052. URL https://www.sciencedirect.com/science/article/pii/S016761051930652X.

[36] P. K. Sweby. High resolution schemes using flux limiters for hyperbolic conservation laws. *SIAM Journal on Numerical Analysis*, 21(5):995–1011, 1984. doi: 10.1137/0721062. URL https://doi.org/10.1137/0721062.

[37] Yong Cao and Tetsuro Tamura. Large-eddy simulations of flow past a square cylinder using structured and unstructured grids. *Computers & Fluids*, 137:36–54, 2016. ISSN 0045-7930. doi: https://doi.org/10.1016/j.compfluid.2016.07.013. URL https://www.sciencedirect.com/science/article/pii/S0045793016302225.

[38] Jing Jiang, Jingyu Liu, Zijin Li, Tingyu Zhang, and Hong Yang. Analysis on the mechanism of sound production and effects of musical flue pipe. *Cognitive Computation and Systems*, 4(1):77–84, 2022. doi: https://doi.org/10.1049/ccs2.12048. URL https://ietresearch.onlinelibrary.wiley.com/doi/abs/10.1049/ccs2.12048.

Abstract in lingua italiana

Il campo aeroacustico di una canna d'organo viene studiato da un punto di vista numerico, risolvendo le equazioni di Navier-Stokes comprimibili e modellando la turbolenza con Large Eddy Simulation utilizzando la libreria open source OpenFOAM e l'analogia acustica di Ffowcs Williams e Hawkings. L'obiettivo della tesi è quello di eseguire una simulazione di un modello tridimensionale di una canna d'organo. Per valutare la metodologia viene studiato il rumore indutto da un flusso laminare su un cilindro quadrato, confrontando i risultati con Inoue *et al.*. Per validare i risultati sulla canna d'organo viene utilizzato un modello bidimensionale, riprendendo il lavoro di Fischer *et al.*. Il caso bidimensionale viene utilizzato anche per studiare i meccanismi fluido dinamici che generano il suono, concentrandosi sull'accoppiamento e sui cambiamenti di comportamento dovuti a modifiche della geometria. I risultati ottenuti dal modello tridimensionale vengono confrontati con il caso bidimensionale. Gli spettri SPL del campo acustico lontano sono ottenuti utilizzando un'analogia acustica e confrontati con le misurazioni su canne d'organo reali.

Parole chiave: Aeroacustica, OpenFOAM, canne d'organo, Ffowcs Williams and Hawkings, FWH, 3D, CFD, Formulazione LES, libAcoustics

Acknowledgements

First and foremost, I would like to thank Professor Paolo Schito for providing me the opportunity to complete this thesis in the field of aeroacoustics. Furthermore, I'd like to thank PhD candidate Alberto Artoni for his tremendous assistance and availability in providing timely feedback with his knowledge in every type of problem that I had to face.
Finally, I would like to thank my family and my friends for their continuous support all this years.